Developments in Perturbative QCD: Challenges from Collider Physics *

Dieter Zeppenfeld

Department of Physics, University of Wisconsin, 1150 University Ave.
Madison, WI 53706, USA
E-mail: dieter@phenom.physics.wisc.edu

ABSTRACT

The search for new phenomena at hadron colliders requires a good understanding of QCD processes. The analysis of multi-jet signatures in the top quark search at the Tevatron is one example, forward jet-tagging and rapidity gap techniques in the analysis of weak boson scattering events at the LHC will be another important application. These topics are discussed in the context of multi-parton/multi-jet QCD processes. Also described are some of the calculational tools, like amplitude techniques and automatic code generation for tree level processes.

1. Introduction

Ever since the start-up of the S$\bar{\text{p}}$pS at CERN, hadron colliders have represented the high energy frontier in particle physics. Up to this day only they have been able to produce W-bosons at a meaningful rate, even though this situation will change in the summer of 1996 with the running of LEP at an energy of 161 GeV. Top quark physics is another area which will only be accessible to hadron colliders in the forseeable future, namely to $p\bar{p}$ collisions at the Tevatron for the next decade and to pp collisions at the LHC afterwards. Even the construction of an e^+e^- linear collider or a $\mu^+\mu^-$ collider will leave the LHC as the machine with the highest usable center of mass energy and, hence, at the forefront of discovery physics.

The discovery of W and Z bosons at the S$\bar{\text{p}}$pS[1] with their clean leptonic decays may well represent the exception rather than the rule for the observation of new physics at hadron colliders. The top quark search,[2-4] in particular in the $t\bar{t} \rightarrow bW^+\bar{b}W^- \rightarrow \ell^\pm\nu + 4$ jets decay mode, is more representative of the complex signatures which must be searched for in order to discover new particles. The production and decay of squarks and gluinos, for example, would lead to multi-particle final states which would give rise to multiple jets and missing transverse momentum signatures or to final states with several leptons and jets in the case of cascade decays of the supersymmetric particles.[5]

In order to distinguish these new physics signals from Standard Model (SM) backgrounds, typically produced by the emission of extra, hard quarks or gluons in simple

---

*Lectures given at the *VIIIth J. A. Swieca Summer School*, Rio de Janeiro, Brazil, February 6–18, 1995.

electroweak processes, the precise features of these multi-parton production processes must be determined, both for the signals and for the backgrounds. Fortunately, amplitude techniques have been developed over the last 15 years[6–8] which are very well suited for this task and which allow to perform parton level Monte Carlo studies with full tree level matrix elements. These lectures describe some recent uses and some of the developments in this field of QCD multi-parton production processes.

In Section 2 the top quark search at the Tevatron will be discussed as an example, showing why the study of multi-parton processes is needed: in order to establish the signal and to measure the top-quark mass kinematically, the $W + 4$ jets background, with and without b-quarks in the final state, had to be understood. Motivated by this example, Section 3 then provides an introduction into the calculation of multi-jet cross sections. I start with a basic discussion of parton level Monte Carlo programs and then describe a particular amplitude technique, developed by Hagiwara and myself,[8] for the efficient evaluation of partonic cross sections. This technique has been encoded in the HELAS program package[9] and is being used by MadGraph[10] to automatically generate the FORTRAN code for (almost) arbitrary SM transition probabilities. The basic ideas behind these programs will be described.

An important application of multi-parton processes is the study of weak boson scattering at the LHC,[11] which includes Higgs production by weak boson fusion, e.g. the process $qq \to qqH \to qqW^+W^-$. In Section 5 the production and subsequent decay $H \to W^+W^-$ of a heavy Higgs boson will be used as an example to discuss some of the techniques, like forward jet-tagging[12–15] or central jet vetoing,[14,15] which have been developed to distinguish weak boson scattering signals from QCD background processes.

Of particular interest here are the different color structures of weak boson scattering (no color exchange in the t-channel) as compared to typical backgrounds where color is exchanged between the two incident partons. This different color structure leads to very different patterns of radiated gluons.[16,17] In the signal, gluons are emitted at rather low transverse momenta and mainly in the forward and backward directions, leaving a central region with little hadronic activity apart from the Higgs decay products. Typical background processes emit gluons at considerably higher transverse momenta and preferentially in the central region. These differences suggest techniques like a minijet veto[18] or rapidity gaps[17] to enhance the signal versus the backgrounds. They will be studied in Section 5. It is helpful, however, to first consider gluon radiation patterns and the consequences of t-channel color singlet exchange in a simpler environment, namely dijet events at the Tevatron. These topics and the recent observation of rapidity gaps at the Tevatron[19–21] will be discussed in Section 4.

2. Jets in the Top Quark Search

The discovery of the top quark[3,4] at the Fermilab Tevatron provides a beautiful example for the use of hadronic jets as a tool for discovering new particles. Let us have a brief look at the top quark search at the Tevatron from this particular viewpoint: the use of multi-parton cross section calculations as a necessary ingredient in particle searches.

In $p\bar{p}$ collisions at the Tevatron, at a center of mass energy of 1.8 TeV, the top quark is produced via quark anti-quark annihilation, $q\bar{q} \to t\bar{t}$, and, less importantly, via $gg \to t\bar{t}$. Production cross sections have been calculated at next-to-leading order[22] and are expected to be around 4 pb for a top mass of 180 GeV.[23] The large top decay width which is expected in the SM,

$$\Gamma(t \to W^+b) \approx 1.7 \text{ GeV} , \tag{1}$$

implies that the t and $\bar{t}$ decay well before hadronization, and the same is true for the subsequent decay of the W bosons. Thus, a parton level simulation for the complete decay chain, including final parton correlations, is a reliable means of predicting detailed properties of the signal. In order to distinguish the top quark signal, $t\bar{t} \to bW^+ \bar{b}W^-$, from multi-jet backgrounds, the leptonic decay $W \to \ell\nu$ ($\ell = e, \mu$) of at least one of the two final state Ws is required. Since the leptonic decay of both Ws has a branching ratio of $\approx 4\%$ only, the prime top search channel is the decay chain

$$t\bar{t} \to bW^+ \bar{b}W^- \to \ell^\pm\nu \, q\bar{q} \, b\bar{b} , \tag{2}$$

which, within the SM, has an expected branching ratio of $\approx 30\%$. After hadronization each of the final state quarks in (2) may emerge as a hadronic jet, provided it carries enough energy. Thus the $t\bar{t}$ signal is expected in $W + 3$ jet and $W + 4$ jet events[*].

Events with leptonic W decays and several jets can also arise from QCD corrections to the basic Drell-Yan process $q\bar{q} \to W^\pm \to \ell^\pm\nu$. The process $ug \to dggW^+$, for example, will give rise to $W + 3$ jet events and its cross section and the cross sections for all other subprocesses with a W and three partons in the final state need to be calculated in order to assess the QCD background of $W + 3$ jet events, at tree level. $W + n$ jet cross sections have been calculated for $n = 3$ jets[24] and $n = 4$ jets[25] and some of the methods used in these calculations will be discussed in Section 3. As in the experiment, the calculated $W + n$ jet cross sections depend critically on the minimal transverse energy of a jet. CDF, for example, requires a cluster of hadrons to carry $E_T > 15$ GeV to be identified as a jet,[2] and this observed E_T must then be translated into the corresponding parton transverse momentum in order to get a prediction for the $W + n$ jet cross sections.

At this level the QCD backgrounds are still too large to give a viable top quark signal. The situation is improved substantially by using the fact that two of the four final state partons in the signal are b-quarks, while only a small fraction of the $W + n$ parton background events have b-quarks in the final state. These fractions are readily calculated by using $W + n$ jet Monte Carlo programs. There are several experimental techniques to identify b-quark jets, all based on the weak decays of the produced b's. One method is to use the finite b lifetime of about $\tau = 1.5$ ps which leads to b-decay vertices which are displaced by $\gamma c\tau = $ few mm from the primary interaction vertex. These displaced vertices can be resolved by precision tracking, with the aid of their

---

[*]Gluon bremsstrahlung may increase the number of jets further and thus all $W+ \geq 3$ jet events are potential $t\bar{t}$ candidates.
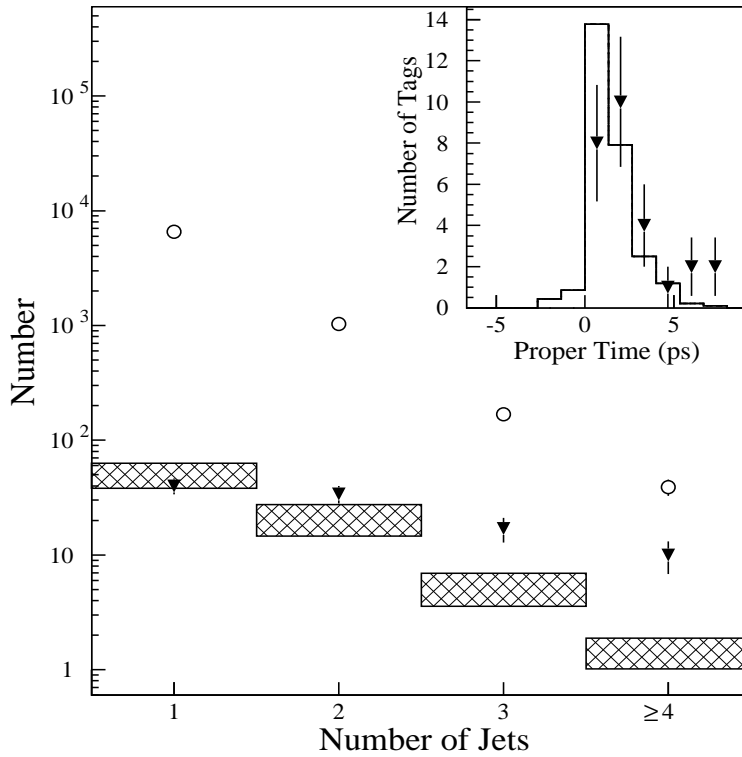
Fig. 1. Number of $W + n$ jet events in the CDF top quark search as a function of jet multiplicity. Number of observed events are given without b-tagging (open circles) and with an SVX tag (triangles). The expected background, mainly from QCD $W + n$ jet events, is given by the cross-hatched bars. From Ref. 3.

Silicon VerteX detector in the case of CDF, and the method is, therefore, called SVX tag. In a second method, b decays are identified by the soft leptons which arise in the weak decay chain $b \rightarrow W^* c$, $c \rightarrow W^* s$, where either one of the virtual Ws may decay leptonically.[2,4]

The combined results of using jet multiplicities and SVX b-tagging to isolate the top quark signal are shown in Fig. 1. A clear excess of b-tagged 3 and 4 jet events is observed above the expected background. The excess events would become insignificant if all jet multiplicities were combined or if no b-tag were used (see open circles). Thus jet counting and the identification of b-quark jets have been critical for the discovery of the top quark.

Beyond counting the number of jets above a certain transverse energy, the more detailed kinematic distributions, their summed scalar E_T's[4] and multi-jet invariant masses, have also been critical in the top quark search and thus needed to be predicted for the $W + n$ jet backgrounds. The top quark mass determination, for example, relies on a good understanding of these distributions. Ideally, in a $t\bar{t} \rightarrow (\ell^+ \nu b)(q\bar{q}\bar{b})$ event, for
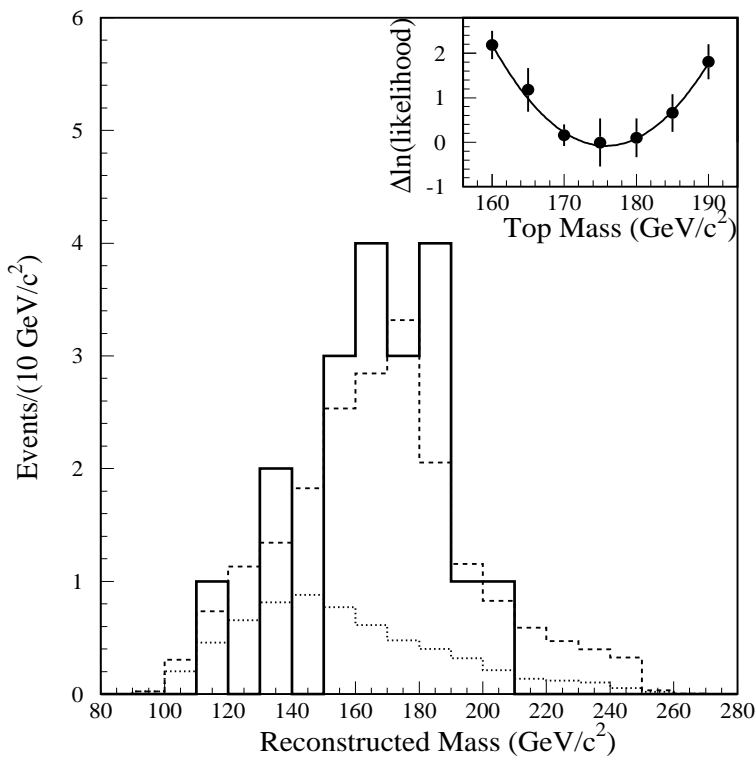
Fig. 2. Reconstructed mass distribution for $W+ \geq 4$ jet events with a b-tag. The solid histogram represents the CDF data. Also included are the expected background (dotted histogram) and the expected signal+background for $m_t = 175$ GeV. The insert shows the likelihood fit to determine the top quark mass, which yielded $m_t = 176 \pm 8 \pm 10$ GeV. From Ref. 3.

example, the two subsystem invariant masses should be equal to the top quark mass,

$$m_t \approx m(\ell^+ \nu b) \approx m(q\bar{q}\bar{b}) \ . \tag{3}$$

Including measurement errors, wrong assignment of observed jets to the two clusters, etc. one needs to perform a constrained fit to extract m_t. The CDF result of this fit[3] is shown in Fig. 2. Combining this with the corresponding D0 measurement[4] gives the value[26]

$$m_t = 180 \pm 13 \text{ GeV} \ . \tag{4}$$

In addition, Fig. 2 demonstrates that the observed b-tagged $W + 4$ jet events (solid histogram) are considerably harder than the QCD background (dotted histogram). On the other hand the data agree very well with the top quark hypothesis (dashed histogram). The kinematic distributions of the jets contain much valuable information and in order to extract it we must be able to reliably calculate them for processes with many partons in the final state.

3. Monte Carlos and Amplitude Techniques

In the previous Section we have seen that the isolation of new physics signals like top quark pair production requires precise predictions for the properties of signal and background processes. One needs to know how the corresponding differential cross sections change as a function of the kinematic variables of the observed leptons and jets. Starting with a generic process

$$p\bar{p} \to B_1 B_2 \ldots B_n X , \qquad (5)$$

where the B_i stand for the final state leptons and jets, we will discuss in the following how to determine the corresponding cross sections in a parton level Monte Carlo program, at tree level. We begin by considering the general structure of a Monte Carlo program in Section 3.1. A formalism for the fast numerical evaluation of polarization amplitudes is described in Section 3.2, and Section 3.3 discusses automatic code generation for the calculation of squared matrix elements, as implemented in the Madgraph[10] program.

3.1. Monte Carlo simulations at the parton level

At the parton level, the process $p\bar{p} \to B_1 B_2 \ldots B_n X$ originates from a number of different subprocesses,

$$a_1 a_2 \to b_1 b_2 \ldots b_n X , \qquad (6)$$

and the cross sections for all these subprocesses must be added to obtain the probability for observing the final state $B_1 B_2 \ldots B_n$.

Consider the $B_1 B_2 = W^+ j$ signature as an example. The contributing parton level subprocesses $a_1 a_2 \to b_1 b_2$ are

$$\bar{d}u, \ \bar{s}c, \ u\bar{d}, \ c\bar{s} \ \to \ W^+ g , \qquad (7)$$
$$ug, \ gu \ \to \ W^+ d , \qquad (8)$$
$$cg, \ gc \ \to \ W^+ s , \qquad (9)$$
$$\bar{d}g, \ g\bar{d} \ \to \ W^+ \bar{u} , \qquad (10)$$
$$\bar{s}g, \ g\bar{s} \ \to \ W^+ \bar{c} , \qquad (11)$$

where Cabibbo mixing has been neglected for simplicity[†]. The various subprocesses are closely related, of course: by choosing either the proton or the anti-proton as the source of the initial state quark or anti-quark, by interchanging first and second generation quark flavors, or by crossing the gluon between the initial and final states. Using these relations, the required analytical calculations can be reduced significantly. At the numerical level, however, only the flavor independence of QCD corrections allows to reduce the number of independent cross section evaluations.

[†]Because of the small value of the Cabibbo angle, $\sin^2\theta_C = 0.049$, the resulting error is negligible compared to the neglect of higher order QCD corrections, for example. It is further mitigated by the fact that after summing over final state flavors and neglecting quark masses, only the annihilation processes (7) depend on the value of the Cabibbo angle.

In order to calculate the cross section for the $B_1 B_2 \ldots B_n$ final state, the squared matrix elements, summed over final state colors and polarizations and averaged over initial ones,

$$\overline{\sum}|\mathcal{M}|^2 = \frac{1}{4} \frac{1}{\#\text{colors}(a_1 a_2)} \sum_{\text{colors}} \sum_{\text{polarizations}} |\mathcal{M}|^2 \qquad (12)$$

must be known for all contributing subprocesses. Their determination is the subject of the next two subsections. The full cross section is then given by

$$\sigma = \int dx_1 dx_2 \sum_{\text{subprocesses}} f_{a_1/p}(x_1) \, f_{a_2/\bar{p}}(x_2)$$

$$\frac{1}{2\hat{s}} \int d\Phi_n(x_1 p + x_2 \bar{p};\ p_1 \ldots p_n)\Theta(\text{cuts})\ \overline{\sum}|\mathcal{M}|^2(a_1 a_2 \to b_1 b_2 \ldots b_n)\ . \qquad (13)$$

Here $f_{a_1/p}(x_1)$ is the probability to find parton a_1 inside the proton, carrying a fraction x_1 of the proton momentum, i.e. the a_1 momentum is $x_1 p$. Similarly, $f_{a_2/\bar{p}}(x_2)$ is the parton a_2 distribution function inside the anti-proton. In the second line of (13) $1/2\hat{s}$ is the flux factor for the partonic cross section, and

$$d\Phi_n(P;\ p_1 \ldots p_n) = \prod_{i=1}^{n} \left(\frac{d^3 \mathbf{p}_i}{(2\pi)^3 2E_i} \right) (2\pi)^4\, \delta^4(P - \sum_i p_i) \qquad (14)$$

is the Lorentz invariant phase space element. Finally, $\Theta(\text{cuts})$ is the acceptance function, which summarizes the kinematical cuts on all the final state particles, i.e. $\Theta = 1$ if all the partons a_i satisfy all the acceptance cuts and $\Theta = 0$ otherwise.

The calculation of the cross section in eq. (13) involves a $3n - 2$ dimensional integral which is best performed by Monte Carlo. In order to do this one first maps the integration region onto a $3n - 2$ dimensional hypercube of unit length, i.e. one rewrites the integration measure as

$$\frac{1}{2\hat{s}} dx_1 dx_2 d\Phi_n = J \prod_{i=1}^{3n-2} dr_i \ , \qquad (15)$$

where J is the Jacobian factor of the transformation of integration variables. The Monte Carlo integration then samples the integrand randomly at some large number, N, of points in the hypercube. In other words, take N sets $\{r_i\}$ of $3n - 2$ random numbers each. A good approximation to the cross section is then provided by

$$\sigma \approx \frac{1}{N} \sum_{\{r_i\}} J \sum_{\text{subprocesses}} f(x_1)f(x_2)\overline{\sum}|\mathcal{M}|^2\, \Theta(\text{cuts})\ , \qquad (16)$$

which approaches the correct cross section value in the limit $N \to \infty$.

Eq. (16) contains all the elements of a Monte Carlo program:

- An integration routine (for example the programs VEGAS[27] or BASES[28]) provides the set $\{r_i\}$ of random numbers and the weight factor $wgt = $ "$1/N$". Each set $\{r_i\}$ is called an event.

- The phase space generator generates the kinematic variables, i.e. the parton momenta p_i, the initial parton momentum fractions x_1 and x_2, and the Jacobian factor J from this set of random numbers.

As a trivial example consider the two body phase space in the decay process $a(P) \rightarrow b_1(p_1)b_2(p_2)$, where b_1 and b_2 represent two massless particles. The Lorentz invariant phase space element is best written in polar coordinates in the P-rest frame:

$$d\Phi_2(P; p_1, p_2) = \frac{1}{32\pi^2} \, d\Omega = \frac{dr_1 \, dr_2}{8\pi} \, , \tag{17}$$

where the components of the 4-momentum p_1 are given by the two random numbers r_1 and r_2 via

$$p_1 = \frac{\sqrt{P^2}}{2}(1, \, \sin\theta\cos\phi, \, \sin\theta\sin\phi, \, \cos\theta) \, , \tag{18}$$

$$\cos\theta = 2r_1 - 1 \, , \quad \phi = 2\pi r_2 \, . \tag{19}$$

Since the phase space element $d\Phi_2$ is Lorentz invariant, the momenta may now be boosted to an arbitrary frame and the momentum p_2 is then calculated from momentum conservation,

$$p_2 = P - p_1 \, . \tag{20}$$

- Given the 4-momenta of the final state particles $\{p_i\}$ one can easily check if the event passes the acceptance cuts, i.e. $\Theta(\text{cuts}) = 1$. If the event is accepted then the squared matrix elements, $\overline{\sum}|\mathcal{M}|^2$, are calculated for all contributing subprocesses.

- The weight factor (value of the integrand)

$$w = J \sum_{subprocesses} f(x_1)f(x_2)\overline{\sum}|\mathcal{M}|^2 \, \Theta(\text{cuts}) \tag{21}$$

is returned to the integration routine, which then adds these weights for the various regions of the hypercube, thus obtaining an estimate of the cross section, σ, according to eq. (16).

- At the same time one can generate arbitrary distributions $d\sigma/dz$ by filling a number of histograms. For each event one uses the 4-momenta p_i to determine the value of z for each histogram in question. Given the bin width Δz one adds $w \cdot wgt/\Delta z$ to the bin corresponding to z and thus obtains a correctly normalized histogram of $d\sigma/dz$ at the end.

In the above procedure the choice of mapping from the unit hypercube to the Lorentz invariant phase space element is obviously ambiguous. The art of writing a good phase space generator is to choose a mapping which results in a large fraction of events having a sizable weight, close to the maximum weight w_{max} encountered in the

full sample. Events with small weights contribute very little to σ in eq. (16) and thus do not reduce the statistical error, but they require as much time to be computed as high weight events. The task in writing the phase space generator is thus to anticipate the dominant phase space regions, those regions in which poles in the matrix elements lead to large cross sections, and to find a mapping which smooths out these maxima in the product $J \overline{\sum} |\mathcal{M}|^2$. It is a good practice to histogram the distribution of the weight factors, w, in order to judge whether improvements to the phase space generator should be made.

3.2.   Amplitude techniques

It is the squared amplitudes, $\overline{\sum} |\mathcal{M}|^2$, which contain the full information on the dynamics of the underlying physical processes and which are at the core of any cross section calculation. For each subprocess $a_1(k_1)\ a_2(k_2) \rightarrow b_1(p_1)\ldots b_n(p_n)$ and phase space point $(k_1, k_2; p_1, \ldots, p_n)$ the squared amplitude has a well defined numerical value. The question then is: What is the most efficient way to "evaluate the Feynman graphs" and to thus obtain this value?

Traditionally, the method of choice has been to use "trace techniques" to express $\overline{\sum} |\mathcal{M}|^2$ in terms of scalar products $p_i \cdot p_j$. For relatively simple processes, like $2 \rightarrow 2$ scattering, one thus obtains very compact and easy to interpret analytical expressions, in particular for unpolarized scattering, and no residual polarization and color sums need to be performed in evaluating Eq. (12) numerically. Unfortunately, the expressions become very large as the number, f, of individual Feynman graphs increases. For

$$\mathcal{M} = \sum_{i=1}^{f} \mathcal{M}_i \tag{22}$$

a total of $f(f+1)/2$ cross terms $\text{Re}(\mathcal{M}_i^* \mathcal{M}_j)$ need to be calculated and hence the complexity of the problem grows at least with the square of the number of Feynman graphs. For $2 \rightarrow 4$ or $2 \rightarrow 5$ processes the task typically becomes forbidding.

For such complex processes the resulting analytical expressions cannot easily be interpreted any more, and in practice one merely needs them for subsequent numerical evaluation. It then becomes advantageous to numerically evaluate the individual Feynman amplitudes $\mathcal{M}_i$ as f complex numbers which can be summed and squared trivially. The complexity of this problem only grows linearly with f.

A number of approaches have been developed for the direct evaluation of polarization amplitudes. The CALKUL method[6] and improvements on it[7] may be the most widely used and it yields rather compact expressions for helicity amplitudes involving massless fermions. Similar (high) numerical speeds are achieved via the HZ method[8] which was developed with massive fermions in mind, but which simplifies significantly as well when massless fermions are considered. As compared to CALKUL results, helicity amplitudes in the HZ method are typically not as compact. However, the basic structure of the underlying Feynman graphs is preserved and this fact has proven invaluable in the automation of code generation.[10] At the same time it becomes very easy

to add new features to existing calculations, like implementing finite width effects[29] or anomalous gauge boson couplings.[30]

The HZ method is implemented in a FORTRAN77 package called HELAS.[9] In the following the principles behind the method will be presented. For full details the reader is referred to the original articles.[8,9]

In order to exploit the simplifications which occur for massless fermions we work in the chiral representation, with γ_5 given by

$$\gamma_5 = \begin{pmatrix} -\mathbb{1} & 0 \\ 0 & \mathbb{1} \end{pmatrix} . \tag{23}$$

External spinors are split into their chiral components,

$$\psi = \begin{pmatrix} \psi_- \\ \psi_+ \end{pmatrix} , \tag{24}$$

where ψ_- and ψ_+ are two-component Weyl spinors of negative and positive helicity, respectively. As an example consider the wave function of an incoming fermion of 4-momentum $p^\mu = (p^0, p_x, p_y, p_z) = (p^0, \mathbf{p})$ and helicity $\sigma/2$. It can be represented by a u-spinor with chiral components

$$u(p, \sigma)_\pm = \sqrt{p^0 \pm \sigma |\mathbf{p}|}\, \chi_\sigma(p) . \tag{25}$$

Here the Weyl spinors of fixed helicity $\sigma/2 = \pm 1/2$ are given explicitly by

$$\chi_+(p) = \frac{1}{\sqrt{2|\mathbf{p}|(|\mathbf{p}| + p_z)}} \begin{pmatrix} |\mathbf{p}| + p_z \\ p_x + ip_y \end{pmatrix} , \tag{26}$$

$$\chi_-(p) = \frac{1}{\sqrt{2|\mathbf{p}|(|\mathbf{p}| + p_z)}} \begin{pmatrix} -p_x + ip_y \\ |\mathbf{p}| + p_z \end{pmatrix} . \tag{27}$$

Given this explicit representation, the four components of the u-spinor can be calculated as a set of four complex numbers once the external 4-momentum and the helicity are fixed. In the HELAS package this is achieved by a simple subroutine call,

```
call IXXXXX(P,FMASS,NH,+1,PSI)
```
where `P=P(0:3)` is the external fermion 4-momentum, `FMASS` is the fermion mass, `NH`$= \sigma = \pm 1$ its helicity, the entry $+1$ indicates that an external fermion (as opposed to anti-fermion) wave function needs to be calculated and the output `PSI = PSI(1:6)` contains the resulting spinor $\psi = u(p, \sigma)$ and the 4-momentum p stored as

$$\mathtt{PSI} = (\psi_1,\ \psi_2,\ \psi_3,\ \psi_4,\ p^0 + ip_z,\ p_x + ip_y) . \tag{28}$$

In the same way the wave function $\overline{v}(p, \sigma)$ of an anti-fermion in the initial state is calculated via

```
call OXXXXX(P,FMASS,NH=σ,−1,PSI)
```

where the entry -1 indicates that the wave function of an anti-fermion is needed and the name `OXXXXX` refers to the direction of the arrow on the fermion line in the Feynman graph: an outgoing fermion line is considered.

The other wave functions which are needed in the calculation of Feynman amplitudes are the polarization vectors of external vector bosons. Given the 4-momentum $k^\mu = (E, \ k_x, \ k_y, \ k_z) = (E, \mathbf{k})$ of a vector boson of mass m, three independent polarization vectors which satisfy $k \cdot \varepsilon = 0$ are given by ($k_T = \sqrt{k_x^2 + k_y^2}$)

$$\varepsilon^\mu(k,0) \;\; = \;\; \frac{E}{m|\mathbf{k}|}(\mathbf{k}^2/E, \ k_x, \ k_y, \ k_z) \; , \tag{29}$$

$$\varepsilon^\mu(k,1) \;\; = \;\; \frac{1}{|\mathbf{k}|k_T}(0, \ k_x k_z, \ k_y k_z, \ -k_T^2) \; , \tag{30}$$

$$\varepsilon^\mu(k,2) \;\; = \;\; \frac{1}{k_T}(0, \ -k_y, \ k_x, \ 0) \; . \tag{31}$$

The polarization vectors for fixed helicities $\lambda = \pm 1$ are obtained from this Cartesian basis via

$$\varepsilon^\mu(k, \lambda = \pm 1) = \frac{1}{\sqrt{2}} \left(\mp \varepsilon^\mu(k,1) - i\varepsilon^\mu(k,2) \right) \tag{32}$$

and they are obtained in HELAS via subroutine calls

    `call VXXXXX(K,VMASS,NHEL(= λ),−1,EPS)`

where -1 indicates that the wave function ε^μ for a vector boson in the initial state is to be calculated ($+1$ would be appropriate for calculating the wave function $\varepsilon^{\mu*}$ of a final state vector boson) and as for fermions `EPS=EPS(1:6)` combines the four components of the complex polarization vector with momentum information on the vector boson.

Having determined the external particle wave functions we need to do the γ-matrix algebra corresponding to the fermion lines inside Feynman graphs. For any 4-vector a^μ the contraction with γ_μ, in the chiral representation, can be written as

$$\slashed{a} = a^\mu \gamma_\mu = \begin{pmatrix} 0 & (\slashed{a})_+ \\ (\slashed{a})_- & 0 \end{pmatrix} . \tag{33}$$

Here the 2×2 submatrices $(\slashed{a})_\pm$ are given by

$$(\slashed{a})_\pm = \begin{pmatrix} a^0 \mp a_z & \mp(a_x - ia_y) \\ \mp(a_x + ia_y) & a^0 \pm a_z \end{pmatrix} \tag{34}$$

Now consider external vector bosons attached to a fermion line as depicted in Fig. 3. The external fermion spinor $\psi = \psi(p)$, the first vector boson emission and the fermion propagator of momentum $p - k_1$ give rise to a new four-component spinor,

$$|k_1, \ p > = \frac{i}{\slashed{p} - \slashed{k}_1 - m_f} \slashed{\varepsilon}_1 \left(-ig_L \frac{1 - \gamma_5}{2} - ig_R \frac{1 + \gamma_5}{2} \right) \psi \; , \tag{35}$$
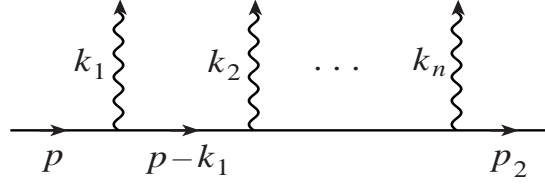
Fig. 3. Piece of a Feynman graph corresponding to vector boson emission off a fermion line.

where the left- and right-handed couplings g_L and g_R depend on the nature of the vector boson considered. In our explicit representation of Dirac-matrices and spinors the resulting ket is obtained by simple 4×4 matrix multiplication which is performed numerically in HELAS via a subroutine call

    call FVIXXX(PSI,EPS1,G,FMASS,0,PSIV)

Here `PSI` and `EPS1` contain the full information on the external spinor and the vector boson of momentum k_1, $G = (-g_L, -g_R)$ stands for the coupling constants, the 0 indicates that the fermion decay width has been set to zero and the output `PSIV = PSIV(1:6)` again stores the four-component spinor $|k_1, p >$ and the 4-momentum $p-k_1$ on the outgoing spinor line, encoded in terms of two complex numbers.

The emission of additional vector bosons now becomes trivial: the output `PSIV` of the last call of `FVIXXX` is used as the input `PSI` of the next `FVIXXX` call, with vector boson 1 replaced by vector boson 2, etc. This leaves us with the last vector boson vertex,

$$\overline{\psi}(p_2)\slashed{\epsilon}_n \left(-ig_L \frac{1-\gamma_5}{2} - ig_R \frac{1+\gamma_5}{2}\right) |k_1, \ldots, k_{n-1}, \ p > , \tag{36}$$

i.e. the task of calculating the final amplitude, corresponding to the Feynman graph of Fig. 3, from the complex 4-spinor $|k_1, \ldots, k_{n-1}, \ p >$, the complex conjugate spinor $\overline{\psi}(p_2)$ and a 4×4 matrix sandwiched in between. This, of course, is a trivial task and accomplished in HELAS by the call of another subroutine, `IOVXXX`. Alternatively, if the last vector boson is virtual, one may want to calculate the 4-vector

$$J^\mu = \frac{i}{k_n^2 - m_V^2} \left(-g^{\mu\nu} + \frac{k_n^\mu k_n^\nu}{m_V^2}\right) \overline{\psi}(p_2)\gamma_\nu \left(-ig_L \frac{1-\gamma_5}{2} - ig_R \frac{1+\gamma_5}{2}\right) |k_1, \ldots, k_{n-1}, \ p > , \tag{37}$$

which can then be used in place of the polarization vector for an external vector boson in e.g. the calculation of a second fermion line. This is done by the subroutine `JIOXXX`.

In an analogous way non-abelian couplings of vector bosons are handled. From the polarization vectors and momenta of two external gauge bosons (or the corresponding currents in the case of virtual gauge bosons) one may calculate a new current (`call JVVXXX`). Alternatively, one can calculate an amplitude from the "wave functions" and momenta of three gauge bosons, via the call of yet another subroutine, `VVVXXX`.

In this fashion numerical expressions for arbitrary Feynman diagrams can be built in a block-like fashion. This method actually is quite economic, since many of the
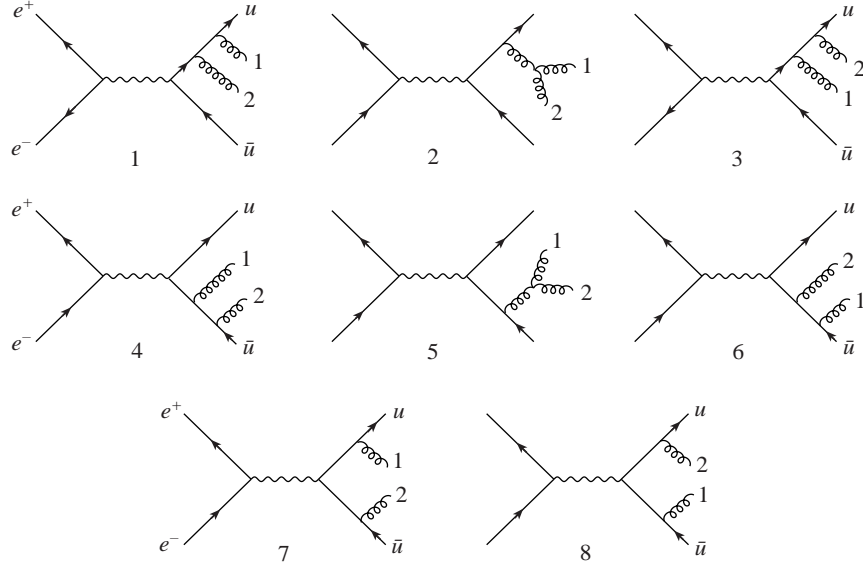
Fig. 4. Feynman graphs for the process $e^+e^- \to \bar{u}ugg$.

building-blocks will be common to several Feynman graphs and only need to be calculated once. As an example consider the Feynman graphs for the process $e^+e^- \to \bar{u}ugg$ depicted in Fig. 4. The incoming e^+e^- current is common to all 8 graphs. Attaching this current to the external v-spinor of the $\bar{u}$ leads to a 4-spinor which is common to graphs 1, 2, and 3. The virtual gluon "current", which describes the 3-gluon vertex, appears in graphs 2 and 5, and so on. Exploiting the repetitive elements in the various Feynman graphs substantially increases the efficiency of the numerical calculation, in particular for processes with a very large number of graphs.

Finally one should mention another convenient feature of the HELAS program. When crossing initial and final state particles the fermion arrows in the Feynman graphs do not change, only the overall signs of the 4-momenta of the crossed particles need to be flipped. This is achieved in HELAS by flipping the sign factors in the determination of the external wave functions: In the `IXXXXX, OXXXXX` and `VXXXXX` calls discussed above the sign of the second last argument needs to be reversed. No further changes are required when calculating crossing related processes.

3.3. Automatic code generation: the MadGraph example

The discussion of the previous subsection should have made it clear that writing the code, which evaluates the squared amplitudes for the various subprocesses, is actually quite a mechanical and boring exercise, exactly the type of task which should be relegated to a computer. Indeed, a number of programs have been developed in recent years for automatic code generation for scattering processes.[31,32] The example to be

discussed below is MadGraph.[10] MadGraph is a standard Fortran program[‡] which generates Fortran code calling the HELAS subroutines. At present MadGraph is capable of generating the code for the squared matrix elements for SM processes with up to seven external particles. It already has been used successfully in state of the art calculations like $Z + 4$ jets production in $p\bar{p}$ collisions.[33]
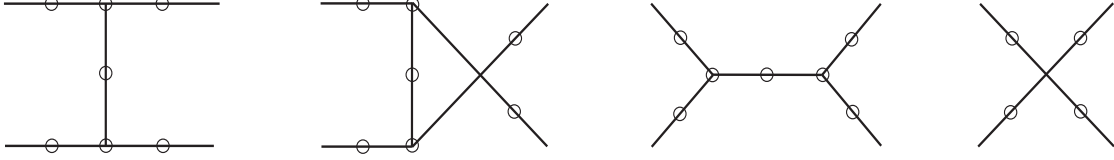

Fig. 5. Allowed topologies for Feynman graphs with four external particles. The circles indicate the 25 locations where a fifth external particle could be attached.

Let us consider the various steps which MadGraph takes to generate a program for the calculation of $\overline{\sum}|\mathcal{M}|^2$. The first step in calculating the scattering amplitude $\mathcal{M}$ is to generate all possible topologies for tree level Feynman graphs, keeping in mind that the SM, as a renormalizable field theory, allows 3 and 4 particle vertices only. As an example, the four possible topologies for Feynman graphs with four external particles are shown in Fig. 5. A fifth external particle could be attached to each of these graphs in the locations indicated by the open circles, leading to 25 distinct tree level topologies for Feynman graphs with 5 external particles. For larger numbers of particles the number of allowed topologies grows very rapidly, as shown in Table 1. This rapid growth leads to increased memory demands of MadGraph and puts a practical limit of 7 external particles on present day workstations.

Table 1. Number of distinct topologies[31] of tree level Feynman graphs in a renormalizable field theory as a function of the number of external particles.

# external particles	3	4	5	6	7	8
# topologies	1	4	25	220	2485	34300

The tree level amplitude is uniquely fixed once the external particles and the interaction lagrangian are specified[§]. In general only a subset of the allowed topologies will actually contribute to a given subprocess. Only the third topology in Fig. 5 contributes to $e^+e^- \to \mu^+\mu^-$, for example, but with two distinct Feynman graphs, corresponding to photon and Z exchange. MadGraph contains a table of all allowed SM

[‡] The MadGraph[10] source code and the HELAS[9] routines called by the Madgraph output can be obtained via anonymous ftp from *phenom.physics.wisc.edu* where it is located in the directory *pub/madgraph/*.

[§] For SM subprocesses involving four or more external quarks both gluon and electroweak boson exchange is possible between the quark lines. In these cases, MadGraph allows the user to choose the desired order in the strong coupling constant α_s.

vertices. For a given topology it first assigns the external particles to the external lines in all permutations. Madgraph then works inwards and checks at each vertex with one unknown line whether there is an allowed assignment of the not yet labeled internal propagator, according to the vertex table. Storing the allowed assignments, the process is continued until either no allowed particle assignment for the last propagator can be found at some vertex or all propagators have been labeled. In the latter case the complete assignment is stored as a Feynman graph which needs to be calculated.

The HELAS code generation follows a similar scheme. First the external particle wave functions are calculated (i.e. the appropriate calls of `IXXXXX`, `OXXXXX` or `VXXXXX` are printed in the output program). The wave functions are, of course, common to all the Feynman graphs. For a vertex with one unknown line, one of the function calls described in the previous subsection then determines the (virtual particle) wave function corresponding to this line, be it a current for a gauge boson or a 4-spinor for a fermion. This procedure ends at a last vertex where all wave functions of the incident particles have been calculated. One final subroutine call then determines the complex value, A_i, of the amplitude for the given Feynman graph.

The A_i only contain the propagator factors, coupling constants and the Lorentz structure of the vertices. For QCD processes the color factors are not yet included. For a given Feynman graph the color factor is a product of factors from each vertex[¶]. These are, for example,

$$q_i \; \bar{q}_j \; g^a \quad \text{vertex}: \qquad T_{ij}^a = \frac{\lambda_{ij}^a}{2} \; , \tag{39}$$

$$g^a \; g^b \; g^c \quad \text{vertex}: \qquad i \; f^{abc} \; , \tag{40}$$

$$g^a \; g^b \; g^c \; g^d \quad \text{vertex}: \qquad -f^{abe} f^{cde} \qquad \text{(3 vertices)} \; , \tag{41}$$

$$q_i \; \bar{q}_j \; \gamma \quad \text{vertex}: \qquad \delta_{ij} \; . \tag{42}$$

In the squared amplitude all colors are summed/averaged over and MadGraph uses the familiar commutator and completeness relations

$$i \; f^{abc} \;\; = \;\; 2 \, \text{tr} T^a [T^b, T^c] \; , \tag{43}$$

$$T_{ij}^a T_{kl}^a \;\; = \;\; \frac{1}{2} \delta_{il} \delta_{kj} - \frac{1}{2N} \delta_{ij} \delta_{kl} \; , \tag{44}$$

to calculate the color summed/averaged products, C_{ij}, of the color factors for any pair of Feynman graphs, i, j. Thus, the squared amplitude takes the form

$$\overline{\sum} |\mathcal{M}|^2 = \sum_{i,j=1}^{f} A_i^* \, C_{ij} \, A_j \; . \tag{45}$$

[¶]Each 4-gluon vertex leads to three distinct Feynman graphs in MadGraph, corresponding to the three different color structures in the Feynman rule

$$- f^{abe} f^{cde} \left(g_{\mu\rho} g_{\nu\sigma} - g_{\mu\sigma} g_{\nu\rho} \right) - f^{ace} f^{dbe} \left(g_{\mu\sigma} g_{\nu\rho} - g_{\mu\nu} g_{\sigma\rho} \right) - f^{ade} f^{bce} \left(g_{\mu\nu} g_{\rho\sigma} - g_{\mu\rho} g_{\nu\sigma} \right) \; . \tag{38}$$

A final trick is then used to simplify the color structure[34]: the hermitian matrix C_{ij} is diagonalized, yielding n_{max} nonzero eigenvalues λ_n and orthogonal eigenvectors z_{nj},

$$\sum_{j=1}^{f} C_{ij} z_{nj}^* = \lambda_n \ z_{ni}^* \ . \tag{46}$$

This allows to write the squared amplitude in terms of a much smaller $n_{max} \times f$ dimensional matrix z and a set of n_{max} eigenvalues λ_n,

$$\overline{\sum}|\mathcal{M}|^2 = \sum_{n=1}^{n_{max}} \lambda_n |\sum_{i=1}^{f} z_{ni} A_i|^2 \ . \tag{47}$$

In MadGraph the eigenvalues λ_n and the z_{ni} are also used to absorb additional factors which appear in the cross section formulas for specific processes:

- A relative factor -1 between subamplitudes which are obtained by interchanging external fermions.

- A factor $1/N!$ for each set of N identical particles in the final state.

- An overall factor $(\# \text{ initial colors})^{-1}$ from taking the average over initial state colors.

These last two factors must be kept in mind when using the simple crossing relations of the HELAS functions to obtain squared amplitudes for crossing related processes: Mad-Graph generates the code for calculating the polarization and color *averaged* amplitude squared for a specific input process.

Using MadGraph actually is very simple, one merely needs to type in the desired process in a self-explanatory shorthand fashion. It is prudent, however, to keep the general MadGraph and HELAS properties in mind, so as to be able to change the generated programs to ones needs. Desired changes may involve the addition of new physics contributions to the amplitudes, a more sophisticated treatment of finite width effects, or a more economic programming of crossing related processes. One should always keep in mind that automated systems are merely intended to free us from the labor of mindless coding. They are tools which make studying the dynamics of multi-parton processes more enjoyable and which allow us to concentrate on all the physics aspects of signal and background processes.

4. Manifestations of Color: Rapidity Gaps at the Tevatron

One important aspect distinguishing signal and background processes is the color flow in the contributing Feynman graphs. Many signal processes involve electroweak interactions and are thus due to the exchange of color singlet quanta while the QCD backgrounds are mediated by color octet gluon exchange. The question arises whether this different color flow has observable consequences which can then be used for background reduction. There is no general answer to this question. However, there is an

important class of processes, mediated by t-channel color singlet exchange, where the answer is a clear "yes". One of the most important fields of study at the LHC, weak boson scattering, belongs to this class and will be addressed in more detail in the next Section. Let us start here with a much simpler example, namely dijet production at the Tevatron, which has emerged as an unexpectedly rich QCD laboratory in recent years. The discussion will closely follow Ref. 35.
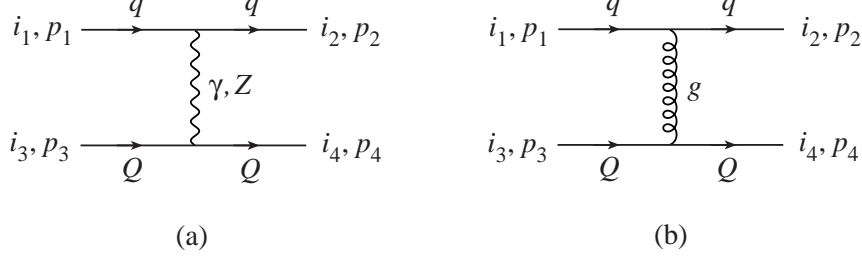

Fig. 6. Feynman graphs contributing to elastic quark-quark scattering via a) color singlet photon or Z exchange and b) color octet gluon exchange.

4.1. Quark-quark scattering at the tree level

A number of $2 \rightarrow 2$ subprocesses contribute to dijet production: gluon-gluon scattering, quark-gluon scattering, $q\bar{q}$ annihilation and pair production, and quark-quark or quark-antiquark elastic scattering. For simplicity let us concentrate on the Rutherford scattering process

$$q_1(p_1, i_1)Q_3(p_3, i_3) \rightarrow q_2(p_2, i_2)Q_4(p_4, i_4) , \tag{48}$$

where the i_n and p_n denote the colors and momenta of the quarks. The two types of SM contributions, namely color singlet γ/Z exchange and color octet gluon exchange in the t-channel are depicted in Fig. 6. Neglecting the Z contribution in the following, the matrix elements for the two cases can be written as

$$\mathcal{M}_\gamma = \delta_{i_2 i_1} \delta_{i_4 i_3} e_q e_Q A = \delta_{i_2 i_1} \delta_{i_4 i_3} e_q e_Q \frac{\overline{u}(p_2)\gamma^\mu u(p_1) \, \overline{u}(p_4)\gamma_\mu u(p_3)}{(p_1 - p_2)^2} , \tag{49}$$

$$\mathcal{M}_g = T^a_{i_2 i_1} T^a_{i_4 i_3} g^2 A = \left(\frac{1}{2}\delta_{i_2 i_3}\delta_{i_4 i_1} - \frac{1}{2N}\delta_{i_2 i_1}\delta_{i_4 i_3} \right) g^2 A . \tag{50}$$

The Kronecker deltas in $\mathcal{M}_\gamma$ describe the fact that the color of q_1 is directly transferred to q_2 while in the QCD case the exchanged gluon transmits the color of q_1 to Q_4 (to leading order in $1/N$). Does this difference in color structure lead to observable consequences?

A qualitative understanding of these differences can be obtained by considering the acceleration of the color charges in forward scattering, at small $|t| = -(p_1 - p_2)^2 = s/2 \, (1 - \cos \theta) << (p_1 + p_3)^2 = s$. In the case of t-channel photon exchange, quark

q will be deflected by a small angle θ with respect to the original q_1 direction and so will the color charge carried by it. The acceleration of the color charge by a small angle results in gluon bremsstrahlung in the forward direction only and, similarly, the small deflection of the color charge carried by Q results in gluon radiation in the backward direction, with very little radiation between the two scattered quarks. For color octet gluon exchange, on the other hand, the color charges are exchanged between the two quarks q and Q, i.e. they are deflected by the large angle $\pi - \theta$, and this strong acceleration of color charges results in strong gluon bremsstrahlung at large angles, between the directions of the final state quarks.
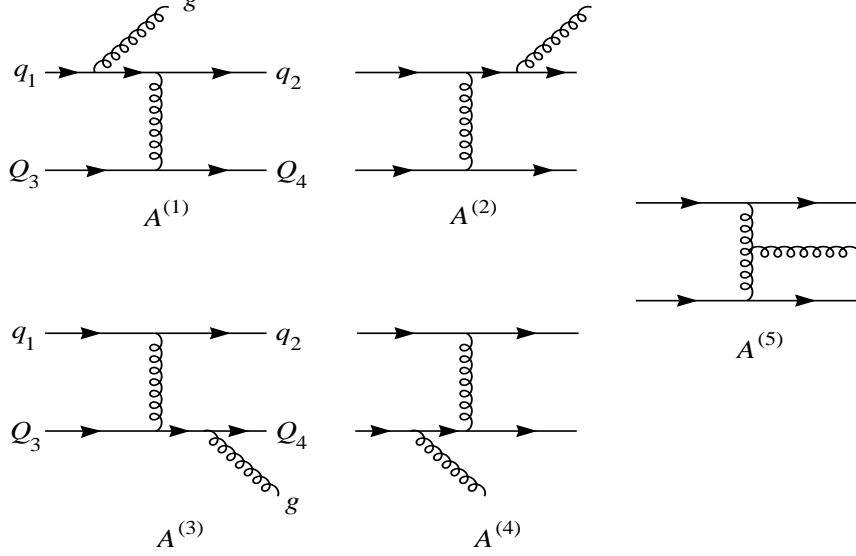

Fig. 7. Feynman graphs for the process $qQ \rightarrow qQg$ at tree level.

This qualitative picture is confirmed by calculating the gluon emission corrections to qQ elastic scattering, i.e. by considering the process

$$q(p_1, i_1)\, Q(p_3, i_3) \longrightarrow q(p_2, i_2)\, Q(p_4, i_4)\, g(k, a) \,, \tag{51}$$

where k and a denote the gluon momentum and color. At any order of perturbation theory, the amplitude for this process can be written in terms of four orthogonal color tensors, which we denote by O_1, O_2, S_{12}, and S_{34},

$$\mathcal{M} = O_1 M_1 + O_2 M_2 + S_{12} M_{12} + S_{34} M_{34} \,. \tag{52}$$

In an $SU(N)$ gauge theory they are given explicitly by

$$
\begin{aligned}
S_{12} &= T^a_{i_4 i_3}\, \delta_{i_2 i_1} & (53) \\
S_{34} &= T^a_{i_2 i_1}\, \delta_{i_4 i_3} & (54) \\
O_1 &= \frac{-2}{N}\, (S_{12} + S_{34}) + T^a_{i_2 i_3}\, \delta_{i_4 i_1} + T^a_{i_4 i_1}\, \delta_{i_2 i_3} & (55) \\
O_2 &= T^a_{i_4 i_1}\, \delta_{i_2 i_3} - T^a_{i_2 i_3}\, \delta_{i_4 i_1} \,. & (56)
\end{aligned}
$$

S_{12} marks the process where the quark q keeps its color. Similarly, S_{34} multiplies the amplitude for t-channel color singlet exchange as viewed from quark Q. Within QCD, O_1 and O_2 correspond to t-channel color octet exchange as viewed from either of the two scattering quarks.

Let us first apply this color decomposition to the tree level QED and QCD amplitudes. The five Feynman graphs for the QCD process are shown in Fig. 7. Lumping the momentum and helicity dependence of the individual Feynman diagrams into reduced amplitudes $A^{(1)} \cdots A^{(5)}$, one obtains for the QCD amplitudes at tree level

$$M_{12}^{\text{QCD}} = \frac{-g^3}{2N} \left(A^{(1)} + A^{(2)} \right) \equiv \frac{-g^3}{2N} A^{(12)} \tag{57}$$

$$M_{34}^{\text{QCD}} = \frac{-g^3}{2N} \left(A^{(3)} + A^{(4)} \right) \equiv \frac{-g^3}{2N} A^{(34)} \tag{58}$$

$$M_1^{\text{QCD}} = \frac{-g^3}{4} \left(A^{(1)} + A^{(2)} + A^{(3)} + A^{(4)} \right) \tag{59}$$

$$M_2^{\text{QCD}} = \frac{-g^3}{4} \left(A^{(1)} - A^{(2)} + A^{(3)} - A^{(4)} + 2A^{(5)} \right) \equiv \frac{-g^3}{4} A^{(\text{na})} . \tag{60}$$

The non-abelian three-gluon-vertex only contributes to the color octet exchange amplitude M_2. Both M_2 and M_1 vanish for t-channel photon exchange, while the color singlet exchange amplitudes are given by

$$M_{12}^{\text{QED}} = -ge_q e_Q \left(A^{(3)} + A^{(4)} \right) = -ge_q e_Q A^{(34)} \tag{61}$$

$$M_{34}^{\text{QED}} = -ge_q e_Q \left(A^{(1)} + A^{(2)} \right) = -ge_q e_Q A^{(12)} , \tag{62}$$

where e_q and e_Q denote the electric charges of the two quarks.

The resulting color and polarization summed squared amplitudes,

$$\sum |\mathcal{M}|^2 = \frac{N^2 - 1}{2} N \sum_{\text{polarizations}} \left(|M_{12}|^2 + |M_{34}|^2 + 2\frac{N^2 - 4}{N^2}|M_1|^2 + 2|M_2|^2 \right) , \tag{63}$$

are shown in Fig. 8(a) for both the QCD and the QED case. Shown is the dependence of $\sum |\mathcal{M}^2|/s$ on the rapidity of the emitted gluon when all other phase space parameters are kept fixed, namely the two quarks are held at $p_T = 30$ GeV and pseudorapidities $\eta_q = 3$ and $\eta_Q = -3$ and the gluon transverse momentum is chosen to be $p_{Tg} = 2$ GeV. The details of this choice are irrelevant: forward scattering of the two quarks is a sufficient condition to obtain the qualitative radiation pattern of Fig. 8. In the QCD case the color octet contributions, via the non-abelian amplitude $A^{(\text{na})}$, lead to enhanced gluon emission in the angular region between the two jets. For t-channel photon exchange this region is essentially free of gluons due to color coherence between initial and final state gluon radiation[36,37]: gluon emission into the central region is exponentially suppressed as the rapidity distance from the quarks increases.

Going beyond the parton level scattering process and considering the actual $p\bar{p}$ scattering event, hadronization of the emitted gluons will result in (soft) hadrons which
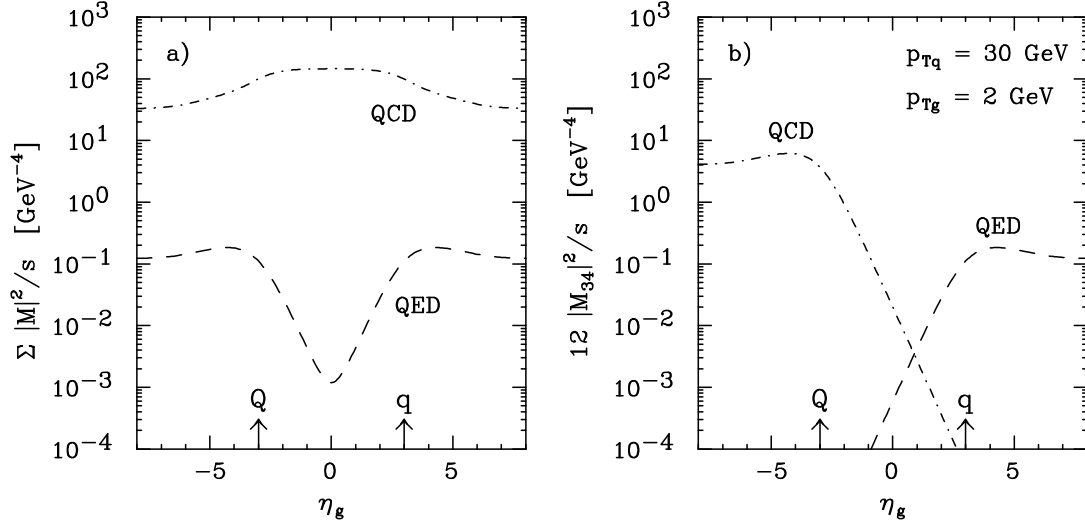
Fig. 8. Rapidity distribution of emitted gluons in $qQ \to qQg$ scattering for fixed final state parton transverse momenta of $p_{Tq} = 30$ GeV and $p_{Tg} = 2$ GeV. The quark rapidities are fixed at $\eta_q = \pm 3$ (indicated by the arrows). In part a) results are shown for the sum over all color structures for single gluon and for t-channel photon exchange. The M_{34} terms alone, in part b), demonstrate the difference between the QED and the QCD color singlet exchange terms. Quark charges are taken as $e_q = e_Q = +2/3e$.

will trace the angular distribution of their parent partons. In t-channel color singlet exchange, gluon radiation is severely suppressed in the angular region between the quarks, and, thus, a similar pattern of soft hadrons is expected. This leaves a rapidity gap, i.e. a rapidity region between the two quark jets which is essentially void of produced hadrons.

4.2. Rapidity gaps at the Tevatron

Rapidity gaps in hard dijet events have indeed been observed at the Tevatron.[19–21] The D0 Collaboration, for example, has studied events with two hard, forward and backward jets with

$$E_T > 30\,\text{GeV}\,, \qquad |\eta_j| > 2\,, \qquad \eta_1 \cdot \eta_2 < 0\,, \tag{64}$$

and has then searched for signs of hadronic activity in the pseudorapidity range between the two jets. Inside the region of width $\Delta\eta_c$ between the tangents to the two jet definition cones (of radius $R = 0.7$ in the lego-plot) D0 has then studied the hadronic multiplicity in terms of the number of active towers in the electromagnetic calorimeter, above a minimum transverse energy threshold of 200 MeV. The measured multiplicity distribution is shown in Fig. 9. One observes a clear excess of low multiplicity events, above the expectation from extrapolating a double negative binomial distribution which

fits very well the high multiplicity region. This excess corresponds to a fraction

$$f_{gap} = 1.07 \pm 0.10(\text{stat})^{+0.25}_{-0.13}(\text{syst}) \% \qquad (65)$$

of rapidity gap events in dijet production. In addition, this fraction is essentially independent of $\Delta\eta_c$, for pseudorapidity separations larger than $\Delta\eta_c \approx 2$ between the jet definition cones.[19] This independence of scattering angle in the parton c.m. frame (for forward scattering) implies that the rapidity gap events follow a $1/t^2$ Rutherford scattering distribution, just like the non-gap dijet events to which they are normalized and which are dominated by single gluon exchange in the t-channel.
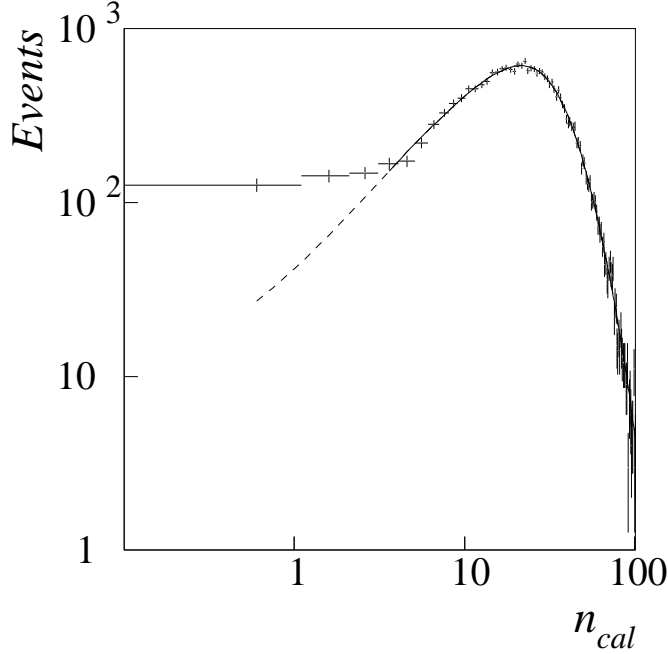

Fig. 9. Electromagnetic tower multiplicity between widely separated jets as observed by D0.[21] Because of the logarithmic n_{cal} scale all multiplicities are shifted by +0.5 to the right. The excess of low multiplicity (rapidity gap) events above the double negative binomial fit (solid and dashed line) is due to color singlet exchange in the t-channel.

This angular distribution is exactly as would be expected if the gap events were produced by t-channel photon exchange. However, the observed rate is too large to be consistent with an electroweak origin. The dijet cross section from t-channel photon, Z or W exchange is between 10^{-3} and 10^{-4} of the QCD dijet cross section[38] in the phase space region considered by D0 and, hence, cannot account for the one percent fraction of dijet events which exhibit a rapidity gap.

Actually, the discrepancy is even larger because a rapidity gap, even if present at the level of a single parton collision, may be covered by double parton scattering (DPS) or, more generally, the underlying event. The hardness of the produced jets translates

into an impact parameter between the scattering partons which is negligible compared to the transverse size of the incident protons. This makes it quite likely that some of the other partons in the p and the $\bar{p}$ will scatter as well, via gluon (color) exchange, and the resulting color recombination would lead to the filling of the rapidity gap. Only the fraction of dijet events without DPS or an underlying event can be expected to preserve a rapidity gap. This fraction, the survival probability P_s of rapidity gaps, has been estimated by several authors[17,37,39] for both the Tevatron and supercolliders and it is expected to be in the 3–30% range. For illustration I will use a value of $P_s = 10\%$ in the following. At the LHC P_s can be measured independently, by comparing the number of electroweak $qq \to qqW$ or $qq \to qqZ$ events which exhibit a rapidity gap with the SM cross sections for these processes.[40]

4.3. Two gluon color singlet exchange and rapidity gaps

Given that electroweak quark scattering cannot account for the observed rate of rapidity gap events at the Tevatron, there must be a QCD source of t-channel color singlet exchange. Indeed, the exchange of two gluons in a color singlet state, as depicted in Fig. 10(b), provides a ready source and has been suggested by Low and Nussinov as the basic model for the Pomeron.[41]
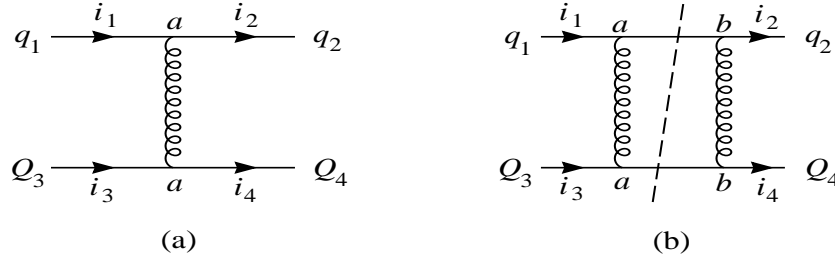

Fig. 10. Feynman graphs for quark scattering via (a) single gluon exchange and (b) exchange of two gluons in a color singlet state.

The rate of rapidity gap events can be understood qualitatively in terms of forward scattering by single gluon and two gluon color singlet exchange as shown in Fig. 10. The observed rate was, in fact, predicted by Bjorken.[17] For forward qq scattering the matrix elements for the dominant helicity configurations are given by

$$\mathcal{M}_g \approx \frac{8\pi\alpha_s \hat{s}}{Q^2} \, T^a_{i_2 i_1} \, T^a_{i_4 i_3} \tag{66}$$

for single gluon exchange, while color singlet two gluon exchange is dominated by the imaginary part of the amplitude in the forward region,

$$
\begin{aligned}
\mathcal{M}_{singlet} \; &\approx \; i \, \frac{8\pi\alpha_s \hat{s}}{Q^2} \, \frac{\alpha_s}{2} \log(Q^2 R^2) \; \left((T^b T^a)_{i_2 i_1} \, (T^b T^a)_{i_4 i_3} \right)_{singlet} \\
&= \; i \, \frac{8\pi\alpha_s \hat{s}}{Q^2} \, \frac{\alpha_s}{2} \log(Q^2 R^2) \; \mathrm{tr}(T^b T^a)\frac{\delta_{i_2 i_1}}{3} \, \mathrm{tr}(T^b T^a)\frac{\delta_{i_4 i_3}}{3} \; .
\end{aligned}
\tag{67}
$$

22

Here R is a cutoff parameter, of the order of the proton radius, which is needed because the intermediate phase space integral for the Feynman graph in Fig. 10(b) is infrared divergent. The fraction of two gluon color singlet exchange events is then given by

$$
\begin{aligned}
\frac{\hat{\sigma}_{singlet}}{\hat{\sigma}_g} &= \frac{\frac{4}{9}|\mathrm{Im}\mathcal{M}_{singlet}|^2}{2|\mathcal{M}_g|^2} = \frac{2}{9}\left|\frac{1}{2}\log(Q^2 R^2)\,\alpha_s(Q^2)\right|^2 \\
&\approx \frac{2}{9}\left|\frac{1}{2}\log(Q^2 R^2)\,\frac{12\pi}{(33-2n_f)\,\log\frac{Q^2}{\Lambda_{QCD}^2}}\right|^2 ,
\end{aligned}
\tag{68}
$$

where we have used the LO formula for the running coupling constant at the scale Q^2 which is the physical scale of the process. For sufficiently large momentum transfer $Q^2 = |\hat{t}|$ the two logs are approximately equal and one finds a constant color singlet exchange fraction,

$$
\frac{\hat{\sigma}_{singlet}}{\hat{\sigma}_g} \approx \frac{1}{2}\left|\frac{4\pi}{33-2n_f}\right|^2 \approx 0.15 ,
\tag{69}
$$

for $n_f = 5$. Thus about 15% of all quark-quark scattering events are due to color singlet two gluon exchange and may lead to a rapidity gap, provided that no underlying event is present. The probability for the latter is given by the survival probability P_s and thus the expected fraction of dijet events from quark-quark scattering with an observable rapidity gap is expected to be[17]

$$
f_{qq} = \frac{d\sigma_{qq,gap}/dt}{d\sigma_{qq,dijet}/dt} \approx 0.15\,P_s \approx 0.015 ,
\tag{70}
$$

which agrees well with the D0 value of 0.0107. This agreement, however, is at least partially by accident. In the forward scattering region, the imaginary parts of the color singlet exchange amplitudes in quark-gluon and gluon-gluon scattering are the same as the quark-quark scattering amplitude, except for a color factor,[17]

$$
\mathrm{Im}\,\mathcal{M}_{gg,singlet} = \frac{9}{4}\,\mathrm{Im}\,\mathcal{M}_{qg,singlet} = \left(\frac{9}{4}\right)^2\mathrm{Im}\,\mathcal{M}_{qq,singlet} ,
\tag{71}
$$

and, at small t, the same proportionality is found for the single gluon exchange cross sections,

$$
\frac{d\sigma_{gg}}{dt} = \frac{9}{4}\frac{d\sigma_{qg}}{dt} = \left(\frac{9}{4}\right)^2\frac{d\sigma_{qq}}{dt} .
\tag{72}
$$

Since the singlet exchange cross section is proportional to $(\mathrm{Im}\,\mathcal{M}_{singlet})^2$, the gap fractions for the three channels are related by

$$
f_{gg} \approx \frac{9}{4}f_{qg} \approx \left(\frac{9}{4}\right)^2 f_{qq} ,
\tag{73}
$$

and, thus, the fraction of color singlet exchange events is substantially larger than the 15% expected for quark-quark scattering alone. Using the measured rapidity gap

fraction of $\approx 1\%$ this in turn indicates a survival probability well below 10% for the Tevatron.

The rate estimates above assume that two gluon color singlet exchange, i.e. the exchange of a Low-Nussinov pomeron, does indeed lead to the same kind of gluon radiation pattern as t-channel photon exchange and, thus, can produce a rapidity gap after hadronization. However, the intermediate phase space integral for the Feynman graph of Fig. 10(b) is dominated by the phase space region where one of the exchanged gluons is very soft. Thus the color of the other, hard gluon is screened at large distances, i.e. the Low-Nussinov pomeron is an extended object with colored constituents. As a result, analogy to single photon exchange may be misleading: gluon radiation may resolve the internal color structure of the pomeron. In order to answer this question we need to find out whether real gluon emission in Low-Nussinov pomeron exchange follows the pattern typical for t-channel gluon exchange or photon exchange.[35] Only in the second case can we expect Low-Nussinov pomeron exchange to lead to rapidity gaps.

We already have studied the general color structure of the process $q_{i_1}Q_{i_3} \rightarrow q_{i_2}Q_{i_4}g^a$. The amplitude contains two color octet pieces M_1 and M_2 and the color singlet exchange amplitudes M_{12} and M_{34}. Let us concentrate on the last one, which describes color singlet exchange as seen by quark Q. Even for t-channel gluon exchange does this color singlet amplitude exist. However, the rapidity distribution of the emitted gluon is markedly different from photon exchange.

In the QED case the M_{34} amplitude corresponds to emission of the final state gluon off the quark q ($A^{(1)}$ and $A^{(2)}$ in Fig. 7). In forward scattering ($\eta_q = +3$ in Fig. 8(b)) the gluon is radiated between the initial and final state q directions, i.e. at $\eta_g \gtrsim \eta_q$. The color i_1 of the initial quark q is thus transferred to a low mass color triplet object which emerges close to the beam direction. At lowest order this is the final state q, at $\mathcal{O}(\alpha_s)$ it is the qg system. The situation is thus stable against gluon emission at even higher order for the QED case and gluon radiation is suppressed in the rapidity range between the two final state quarks.
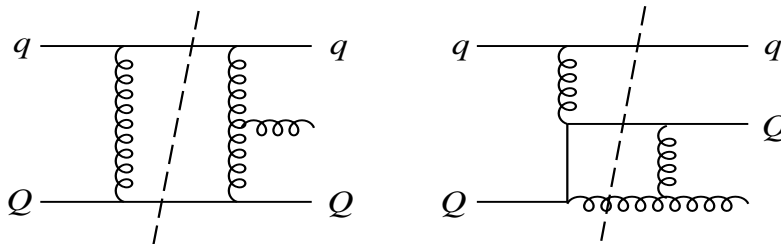

Fig. 11. Two of the 31 Feynman graphs contributing to the imaginary part of the color singlet exchange amplitude M_{34}.

In the QCD case M_{34} corresponds to emission of the gluon from the quark Q. The gluon is preferentially emitted between the initial and the final Q directions, at $\eta_g \lesssim \eta_Q$ (dash-dotted line in Fig. 8(b)). Thus the color triplet qg system, into which the

initial quark q evolves, consists of a widely separated quark and gluon. Higher order corrections will lead to strong gluon radiation into the angular region between the two and thus also into the rapidity range between the two final state quarks.

These typical patterns found for t-channel color singlet and color octet exchange can now be used as a gauge for the radiation pattern produced in $qQ \rightarrow qQg$ scattering via the exchange of two gluons in a color singlet state. In the lowest order process, $qQ \rightarrow qQ$, the color singlet exchange amplitude is dominated by its imaginary part.[42] Hence, we may estimate the radiation pattern by calculating the imaginary part of the gluon emission amplitude M_{34} only. Typical Feynman graphs are shown in Fig. 11. Details of the calculation are given in Ref. 35.

For massless internal gluon propagators the phase space integrals over the qQ, qg, and gQ intermediate states are divergent. They can be regularized by replacing the massless gluon propagator by a version which avoids unphysical gluon propagation over long distances.[43] QCD Pomeron models of this kind have been found to give a good description of available data.[44] These refinements are approximated by using an effective gluon mass of $m_r = 300$ MeV in the calculation.

A second problem arises because some of the contributions to $\text{Im}M_{34}$ correspond to $q \rightarrow g$ splitting and subsequent $gQ \rightarrow gQ$ scattering via pomeron exchange. These contributions cannot be expected to be suppressed when the gluon is emitted between the q and the Q directions and thus would mask the radiation off pomeron exchange in qQ scattering. These splitting contributions have been subtracted in Ref. 35 to yield the square of the pomeron exchange radiation pattern, $|\text{Im}M_{34}^{\text{pom}}|^2$, which is shown in Fig. 12.

For high transverse momentum of the emitted gluon (of order of the quark momenta, see Fig. 12(b)) the radiation pattern is quite similar to the one obtained for single gluon exchange. Hard emitted gluons have too short a wavelength to see the screening of the color charge of the harder exchanged gluon by the second, typically very soft, exchanged gluon. The Low-Nussinov pomeron thus reveals itself as an extended object. Hard gluon emission is able to resolve the internal color structure of the pomeron. As the transverse momentum of the emitted gluon is decreased, a qualitative transition occurs, as is apparent by comparing the $p_{Tg} = 2$ GeV and 15 GeV cases in Fig. 12. The gluon radiation has too long a wavelength to resolve the internal color structure and hence the pomeron appears as a color singlet object.

In dijet production at the Tevatron, in the kinematic range studied by D0, gluon radiation will be dominated by the soft region, with transverse gluon momenta in the few GeV range or below, as shown in Fig. 12(a). The emission of these soft gluons follows a pattern very similar to the one observed for t-channel photon exchange, which leads to the formation of rapidity gaps. One concludes that two gluon color singlet exchange in dijet events does indeed lead to the formation of rapidity gap events as observed at the Tevatron.

5. Weak Boson Scattering

One of the major reasons for building a hadron supercollider is the study of weak boson interactions in the TeV range. Within the forseeable future this task will have
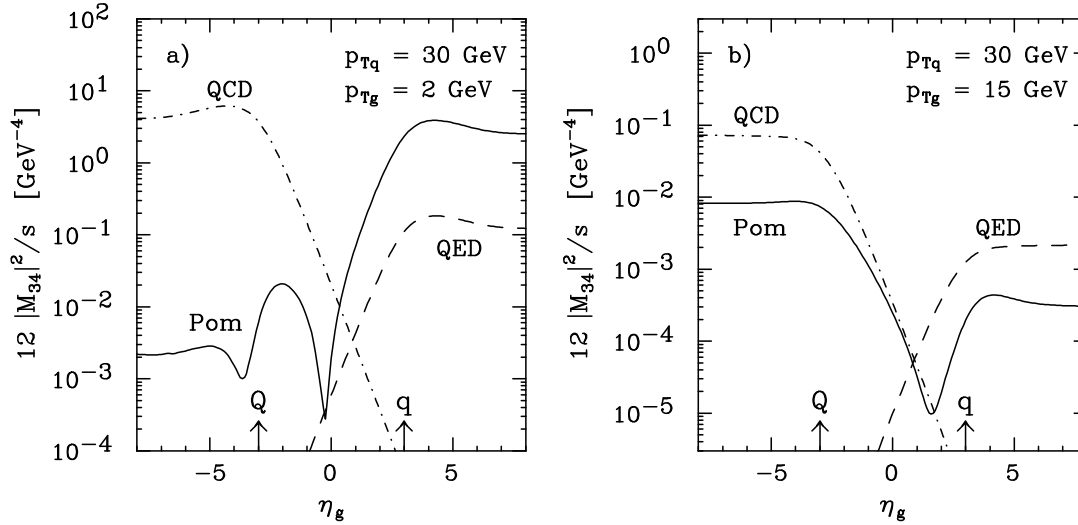
Fig. 12. Rapidity distribution of emitted gluons in $uc \to ucg$ scattering via two gluon color singlet exchange as seen by the charm quark. The phase space parameters for the quarks are the same as in Fig. 8 and results are shown for a) the case of a soft gluon ($p_{Tg} = 2$ GeV) and b) a hard gluon ($p_{Tg} = 15$ GeV). For comparison tree level results are shown for gluon (dash-dotted lines) and photon exchange (dashed lines).

to be performed in pp collisions at 14 TeV at the Large Hadron Collider (LHC) at CERN. Because of its limited energy the study of weak boson scattering will be a very demanding task at the LHC, requiring a full arsenal of tools to isolate $qq \to qqVV$ weak boson scattering events from the backgrounds. For example, jets will have to be used as a tagging device (as in the top quark search at the Tevatron) and rapidity gap techniques, i.e. the exploitation of the t-channel color singlet exchange in the signal, should prove useful as well, thus combining the ideas discussed in the previous Sections. Before considering the benefits of these techniques in weak boson scattering and the search for a heavy Higgs at the LHC, let us start with a brief note on the physics of a strongly interacting Higgs sector.

5.1. Higgs production and longitudinal weak boson scattering[45]

In a more general context, the search for the Higgs boson is part of the quest for the basic interactions which are responsible for the spontaneous breaking of the $SU(2) \times U(1)$ gauge symmetry. The existence of this local symmetry is evidenced by the observation of W and Z bosons and the fact that their experimentally determined couplings to quarks and leptons agree with the gauge theory predictions. The appearance of gauge boson masses then requires the gauge symmetry to be broken spontaneously, with some order parameter Φ acquiring a vacuum expectation value (v.e.v.). The fact that the W to Z mass ratio leads to a ρ-parameter very close to unity finally tells us that this order parameter must transform essentially as an $SU(2)$-doublet.

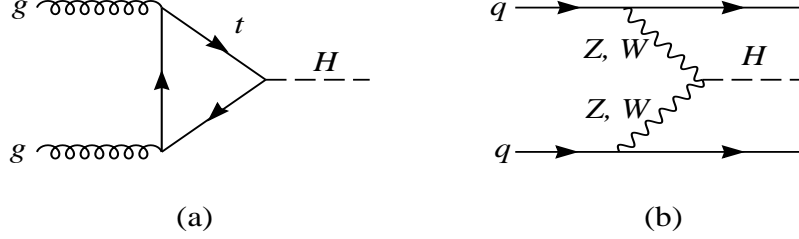Beyond these basic facts the precise nature of the order parameter and of the

Fig. 13. Feynman graphs for the two dominant Higgs production processes at the LHC, (a) gluon-gluon fusion via a top-quark loop and (b) weak boson fusion.

interactions which drive its v.e.v. must be determined experimentally. Within the SM the order parameter is simply the scalar Higgs doublet field,

$$\Phi = \begin{pmatrix} \frac{1}{\sqrt{2}} (v + H + i\chi^3) \\ i\chi^- \end{pmatrix},$$

(74)

where v is the Higgs v.e.v., $\chi^\pm$ and χ^0 are the Goldstone bosons which are closely related to the longitudinal degrees of freedom of the $W^\pm$ and the Z, and H is the field describing the physical Higgs boson which we would like to detect experimentally.

Without spontaneous breakdown of the symmetry, $SU(2) \times U(1)$ gauge invariance forbids any mass terms for the known quarks and leptons as well as for the gauge bosons. Thus these masses must be proportional to the v.e.v. Since v appears only in the combination $v + H$ in the SM (see Eq. (74)), this implies couplings of the fermions and gauge bosons to the Higgs which are proportional to the masses of the former. Let us consider the most important of these, the couplings of the Higgs to the gauge bosons and to the top quark. They are derived from the kinetic energy term for the Higgs doublet field and from the Yukawa coupling of the Higgs field to the top-bottom doublet, $T = (t_L, b_L)^T$, and the right handed top quark field, t_R,

$$
\begin{aligned}
\mathcal{L} &= (D_\mu \Phi)^\dagger (D^\mu \Phi) - (\lambda_t \, \overline{T} \Phi \, t_R + \text{h.c.}) \\
&= \left(1 + \frac{H}{v}\right)^2 \left| \frac{i}{2} \begin{pmatrix} g \, W_\mu^3 - g' \, B_\mu & \cdots \\ g\sqrt{2}W_\mu^- & \cdots \end{pmatrix} \begin{pmatrix} \frac{v}{\sqrt{2}} \\ 0 \end{pmatrix} \right|^2 - \left(1 + \frac{H}{v}\right) \lambda_t \, \overline{t}_L \frac{v}{\sqrt{2}} \, t_R + \ldots \\
&= \left(1 + \frac{H}{v}\right)^2 \left(m_W^2 \, W_\mu^\dagger W^\mu + \frac{m_Z^2}{2} Z_\mu Z^\mu \right) - m_t \, \overline{t}_L t_R \left(1 + \frac{H}{v}\right) + \ldots \,,
\end{aligned}
$$

(75)

which gives relations between the masses and coupling constants,

$$m_W = \frac{gv}{2} \,, \qquad m_Z = \frac{gv}{2 \cos \theta_W} \,, \qquad m_t = \frac{\lambda_t v}{\sqrt{2}} \,.$$

(76)

The interaction terms of Eq. (75) imply that the Higgs boson decays predominantly into the heaviest particles available. For the heavy Higgs scenario, which is considered in the following, these are the decay modes $H \to W^+ W^-$, $H \to ZZ$, and
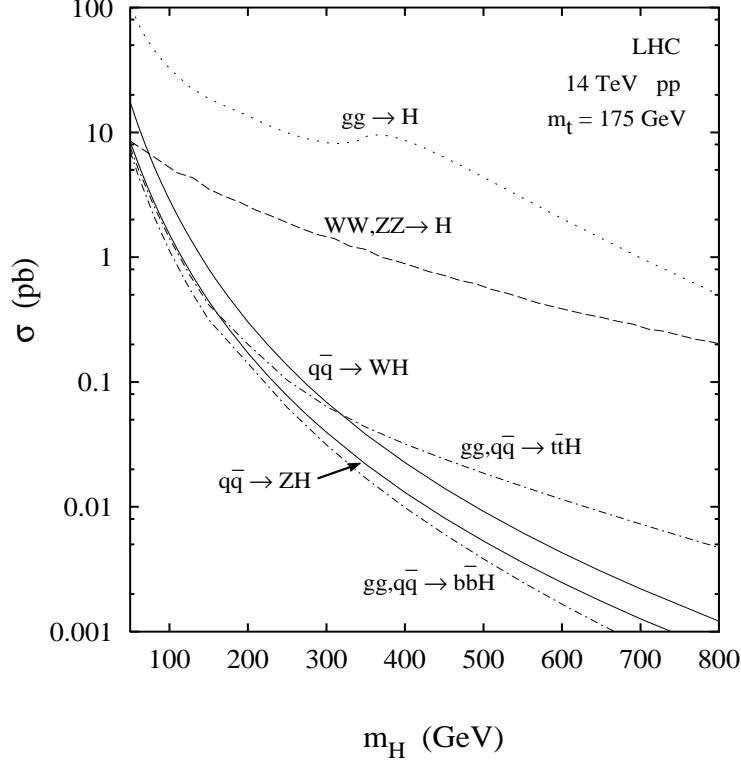
Fig. 14. Production cross sections for the SM Higgs boson at the LHC. From Ref. 46.

$H \to \bar{t}t$. For a Higgs mass of 800 GeV, for example, the corresponding branching ratios are

$$B(H \to W^+W^-) \approx 0.59 \ , \qquad B(H \to ZZ) \approx 0.29 \ , \qquad B(H \to \bar{t}t) \approx 0.12 \ , \quad (77)$$

and the total Higgs decay width is expected to be about 290 GeV. In order to exploit the dominant decay modes, one needs to search for the Higgs signal in W^+W^- and ZZ production events at the LHC, with subsequent leptonic decays of at least one of the weak bosons.

Similar to the Higgs decay modes, the dominant production processes involve heavy particles. At LHC energy, the Higgs boson is mainly produced via gluon fusion, $gg \to H$, which proceeds via a top quark loop and is depicted in Fig. 13(a), and via weak boson fusion, $WW, ZZ \to H$, which, more precisely, is the electroweak process $qq \to qqH$ (see Fig. 13(b)). The corresponding production cross sections are shown in Fig. 14.

While the gluon fusion cross section ranges from 30 to 0.5 pb for 100 GeV $< m_H < 800$ GeV, weak boson fusion rates are typically smaller by a factor 2.5 to 10, the difference becoming smallest at large Higgs boson masses. This somewhat smaller cross section, however, is compensated by a number of features which are special to
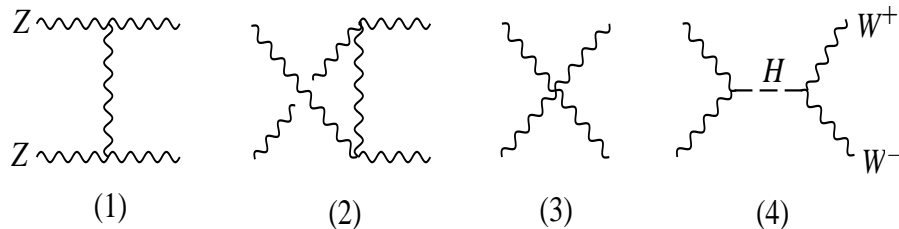
Fig. 15. Feynman graphs for the weak boson scattering process $ZZ \to W^+W^-$.

the weak boson scattering process. First of all the additional two final state quarks will frequently manifest themselves as hadronic jets which allows to suppress backgrounds by jet tagging. Second the two production processes probe different interactions of the Higgs boson. The gluon fusion cross section is proportional to λ_t^2, i.e. it measures the Yukawa coupling of the produced scalar to the top quark. This Yukawa coupling, however, does not identify the produced particle as being connected to the symmetry breaking mechanism, it is possible for a generic scalar particle. The HVV coupling, on the other hand, at tree level, is only possible if H is indeed the Higgs boson. The weak boson fusion rate directly measures the HVV coupling (as does the $H \to VV$ decay width) and thus one would like to measure both gluon and weak boson fusion cross sections in order to disentangle the various couplings of H in Eq. (75).

When considering the full processes $qq \to qqWW$ or $qq \to qqZZ$, the resonance approximation, i.e. considering graph (b) in Fig. 13 only, is only valid for a Higgs width $\Gamma_H \ll m_H$. For a heavy (and wide) Higgs resonance the $VV \to H(\to VV)$ subprocess in Fig. 13(b) must be replaced by the full weak boson scattering amplitude, as depicted in Fig. 15 for the process $ZZ \to WW$. In addition, weak boson bremsstrahlung off the quark lines must be considered.[47,15]

Very strong cancellations between the various Feynman graphs of Fig. 15 appear when all the external vector bosons are longitudinally polarized.[48] The isospin and angular momentum zero contributions from the first two graphs and from the third graph individually grow as $\hat{s}^2/m_W^4$. However, the leading terms cancel when the sum of the three graphs is considered. Even the $\hat{s}/m_W^2$ growth of their sum, however, would lead to a violation of partial wave unitarity at a $\sqrt{\hat{s}}$ of about 1 TeV. At high energies, above $\hat{s} = m_H^2$, it is the destructive interference with the fourth graph, s-channel Higgs exchange, which leads to an acceptable $J = I = 0$ partial wave amplitude. Thus the existence of the Higgs boson, or some other, additional contribution to the weak boson scattering amplitude, beyond the vector boson self-coupling graphs (1)–(3) in Fig. 15, is required by unitarity of the S-matrix.[48] This additional contribution does not have to be the s-channel exchange of a scalar object. It might be the t- or u-channel exchange of a vector particle which resides in a weak isospin triplet, like in technicolor models. Or nature may have realized the unitarization of the weak boson scattering amplitudes in yet another manner.[11]

Depending on which path is realized in nature, the various weak boson scattering

processes like $W^+W^- \to W^+W^-$, $WZ \to WZ$, $W^+W^+ \to W^+W^+$, etc. will exhibit markedly different magnitude and shape (energy dependence) of the cross sections. If a technirho existed, the WZ channel, for example, would exhibit a resonance at the technirho mass, while this channel has a small cross section if a $J = I = 0$ scalar is responsible for the unitarization of the S-matrix (as in the SM). Thus the study of all weak boson scattering channels is important in order to fully probe the symmetry breaking sector. In the following I will use the search for a SM heavy Higgs to discuss techniques of background suppression. One should keep in mind, however, that these methods are more general and can be applied to study any of the weak boson scattering processes.

5.2. Forward jet-tagging

A characteristic feature of weak boson scattering events are the two accompanying quarks (or antiquarks) from which the "incoming" Ws or Zs have been radiated (see Fig. 13(b)). In general these scattered quarks will give rise to hadronic jets. By tagging them, i.e. by requiring that they are observed in the detector, one hopes to obtain a powerful background rejection tool.[12,13] Whether such an approach can be successful depends on the properties of the tagging jets: their typical transverse momenta, their energies, and their angular distributions.

Similar to the emission of virtual photons from a high energy electron beam, the incoming weak bosons tend to carry a small fraction of the incoming parton energy.[49] At the same time the incoming weak bosons must carry substantial energy, of order $m_H/2 = m_{VV}/2$, in order to produce a weak boson pair of large invariant mass. Thus the final state quarks in $qq \to qqVV$ events will carry very high energies, of order 1 TeV or even higher. This is to be contrasted with their transverse momenta, which are of order $p_T \approx m_W$. This low scale arises because the weak boson propagators in Fig. 13(b) introduce a factor

$$D_V(q^2) = \frac{-1}{q^2 - m_V^2} \approx \frac{1}{p_T^2 + m_V^2} \tag{78}$$

into the production amplitudes and suppress the $qq \to qqH$ cross section for quark transverse momenta above m_V. The modest transverse momentum and high energy of the scattered quark corresponds to a small scattering angle, typically in the $1.5 < \eta < 4.5$ pseudorapidity region.

These general arguments are confirmed by Fig. 16, where the transverse momentum and pseudorapidity distributions of the two potential tagging jets are shown for the production of a $m_H = 800$ GeV Higgs boson at the LHC. One finds that one of the two quark jets has substantially lower median p_T (≈ 30 GeV) than the other (≈ 80 GeV). As a result, double jet-tagging, i.e. the requirement that both scattered quarks are visible as jets, proves quite costly[13–15] unless jets with transverse momenta around 30 GeV can be identified in the forward region. A different approach is single forward jet-tagging which relies only on the higher p_T tagging-jet and thus proves more effective for higher transverse momentum thresholds.[14,15,50,51]
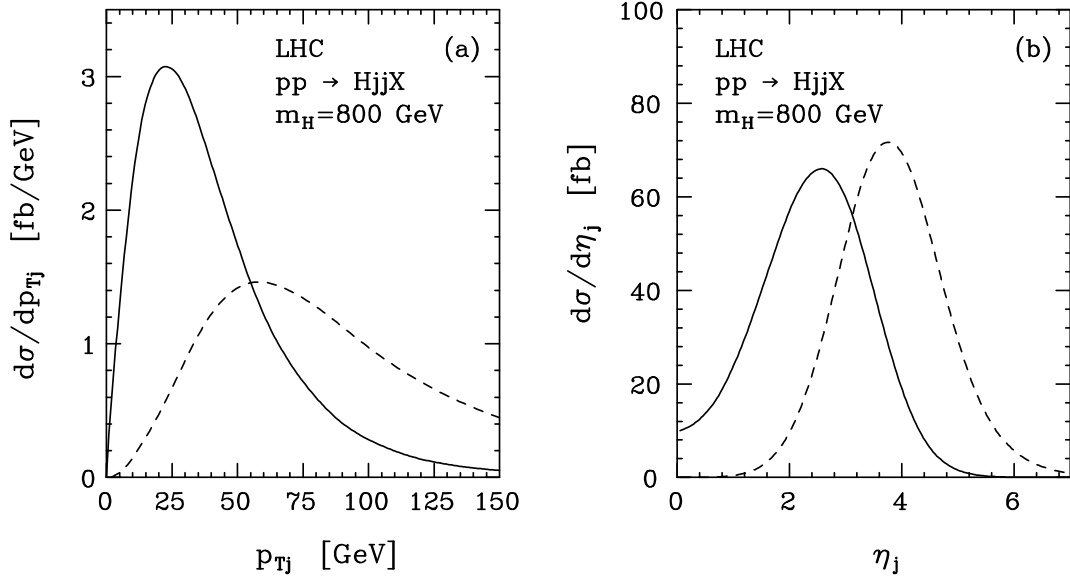
Fig. 16. Transverse momentum and pseudorapidity distributions of the two (anti)quark jets in $qq \to qqH$ events at LHC energy. Shown are (a) $d\sigma/dp_{Tj}$ for the highest (dashed curve) and lowest p_T jet (solid curve) and (b) $d\sigma/d|\eta_j|$ for the most forward (dashed curve) and the most central jet (solid curve).

This transverse momentum threshold needs to be set such that the probability for seeing a fake tagging-jet becomes small. At full LHC luminosity of $\mathcal{L} = 10^{34} \mathrm{cm}^{-2}\mathrm{sec}^{-1}$ one of the most important sources of such background jets are additional $pp \to jjX$ events in the same bunch crossing as the $pp \to VVX$ signal event. With a bunch crossing happening every 25 nsec, a process with a cross section of $\sigma_{eff} = [\mathcal{L}\ 25\mathrm{nsec}]^{-1} = 4$ mb will, on average, happen during each bunch crossing. Using Poisson statistics, the probability to get a random jet of transverse momentum $p_{Tj} > p_{T,\mathrm{cut}}$ in any event previously selected is then given by

$$P_j(p_{T,\mathrm{cut}}) = 1 - \exp\left(-\frac{\sigma_{jj}(p_{Tj} > p_{T,\mathrm{cut}})}{\sigma_{eff}}\right) \approx \frac{\sigma_{jj}(p_{Tj} > p_{T,\mathrm{cut}})}{\sigma_{eff}}\ . \tag{79}$$

With single-jet cross sections of about 0.5–1 mb above $p_{Tj} = 20$ GeV in the relevant rapidity range, overlapping events in a single bunch crossing may produce fake tagging-jets above 20 GeV p_T with about 15–25% probability. This estimate agrees with the results of a more detailed analysis of overlapping events at the LHC.[52]

In the following let us sidestep this question of how low a transverse momentum threshold can be achieved in forward jet-tagging. By restricting ourselves to single forward jet-tagging the jet p_T threshold can be set high enough to avoid the fake jet problem from overlapping events. As an example we will consider the search for $H \to W^+W^- \to \ell^+\nu\ell^-\bar\nu$ decays as discussed in Ref. 18. This particular decay mode

31

suffers from severe backgrounds due to $t\bar{t} \to W^+W^-b\bar{b}$ decays as well as $q\bar{q} \to W^+W^-$ events (referred to as WW QCD background in the following) and thus is well suited to assess the power of jet-tagging and minijet veto techniques.

Since we are interested in the decay of a very heavy Higgs boson, the two charged W decay leptons will emerge with high transverse momentum, in the central region of the detector, and they will be well isolated from additional jets. Thus we require the presence of two charged leptons ($\ell = e, \mu$) with

$$p_{T\ell} > 50 \text{ GeV} , \qquad |\eta_\ell| < 2 , \qquad R_{\ell j} = \sqrt{(\eta_\ell - \eta_j)^2 + (\phi_\ell - \phi_j)^2} > 0.7 . \qquad (80)$$

Here $p_{T\ell}$ denotes the lepton transverse momentum and η_ℓ is its pseudorapidity. The $R_{\ell j} > 0.7$ separation cut forbids a parton (jet) of $p_T > 20$ GeV in a cone of radius 0.7 around the lepton direction.

The lepton p_T cut in Eq. (80) is not in itself sufficient to focus on the production of two W's of large transverse momenta and large W-pair invariant mass. A variable which helps to substantially suppress W bremsstrahlung backgrounds is $\Delta p_{T\ell\ell}$, the difference of the charged lepton transverse momentum vectors.[51] We thus require

$$\Delta p_{T\ell\ell} = |\mathbf{p}_{T\ell_1} - \mathbf{p}_{T\ell_2}| > 300 \text{ GeV} , \qquad m_{\ell\ell} > 200 \, GeV . \qquad (81)$$

The additional cut on the dilepton invariant mass removes possible backgrounds from Z leptonic decays. It is largely superceded by the the $\Delta p_{T\ell\ell}$ cut, however.

Cross sections for events satisfying the lepton acceptance criteria of Eqs. (80,81) are listed in the first column of Table 2 for the case of a $m_H = 800$ GeV Higgs boson and the $q\bar{q} \to W^+W^-$ and $t\bar{t}$ production backgrounds. In the calculation of the $qq \to qqWW$ signal all W bremsstrahlung graphs have been included[47,15] since the narrow Higgs width approximation is not appropriate any more for the large masses considered here. These additional graphs introduce an "electroweak background" which is the same as in the case of a light Higgs boson. Since a light Higgs cannot decay via $H \to WW$, we can use the SM $qq \to qqWW$ cross section for, say, $m_H = 100$ GeV as an estimate of this electroweak background. The heavy Higgs signal is then defined as $B\sigma_{\text{SIG}} = B\sigma(m_H) - B\sigma(m_H = 100 \text{ GeV})$.

Without any jet-tagging the backgrounds are overwhelming: the top quark background alone exceeds the signal by a factor of 300. How much does this situation improve by forward jet-tagging? A large fraction of the signal (55%) is retained by requiring the existence of a very energetic, forward jet of moderate p_T, in the phase space region

$$E_j^{\text{tag}} > 500 \text{ GeV} , \qquad 1.5 < |\eta_j^{\text{tag}}| < 4.5 , \qquad p_{Tj}^{\text{tag}} > 50 \text{ GeV} . \qquad (82)$$

In addition the tagging-jet should be well separated from the W decay leptons,

$$\min |\eta_j^{\text{tag}} - \eta_\ell| > 1.7 , \qquad (83)$$

Since we are now requiring additional jet activity, the previous background calculations are not sufficient any more. Rather $\mathcal{O}(\alpha_s)$ real emission corrections must be

Table 2. Signal and background cross sections $B\sigma$ (in fb) for the Higgs search in $qq \rightarrow qqWW$, $WW \rightarrow \ell\nu\ell\nu$ events. Results are shown for increasingly stringent cuts. From Ref. 18.

| | lepton cuts only | + tagging jet | + lepton-tagging jet separation | + minijet veto ($p_{T,\mathrm{veto}} = 20$ GeV) |
	[Eq. (80)–(81)]	[Eq. (82)]	[Eq. (83)]	[Eq. (85)]
$WW(jj)$	27.4	1.73	0.57	0.13
$t\bar{t}(jj)$	640	57	25	0.47
$m_H = 100$ GeV	1.18	0.56	0.29	0.18
$m_H = 800$ GeV	3.4	1.79	1.31	0.97
signal:				
$m_H = 600$ GeV				0.78
$m_H = 800$ GeV	2.2	1.23	1.02	0.79
$m_H = 1$ TeV				0.62

considered, i.e. $t\bar{t}j$ production and processes like $q\bar{q} \rightarrow W^+W^-g$ and $qg \rightarrow W^+W^-q$ need to be considered at this level. The signal and background cross sections after the cuts of Eqs. (82) and (83) are listed in the second and third columns of Table 2, respectively. Single forward jet-tagging has reduced the backgrounds by a factor 25–50, while keeping 45% of the signal. This reduction factor is almost sufficient for the WW QCD background, but an additional large suppression factor is needed for the top quark decays. Fortunately, the b-quarks in $t \rightarrow bW$ decay frequently give rise to additional jets and a veto on them,[14] above $p_{Tb} = 25$ GeV, will substantially reduce this background.[15] One needs to be careful, however, since at such low transverse momenta the production of minijets via the emission of additional gluons cannot be neglected at the LHC.

5.3. Rapidity gaps and minijet veto

The most rigorous veto on b-quarks from top decays would be a rapidity gap requirement[16,17] as discussed for dijet events at the Tevatron in Section 4.2. A rapidity gap trigger, i.e. the selection of events without any hadronic activity in some rapidity range around the two charged leptons which arise from the two Ws, would make maximal use of the different color structure of signal and background processes. In a weak boson scattering event no color is exchanged between the initial state quarks. Color coherence between initial and final state gluon bremsstrahlung then leads to a suppression of hadron production in the central region, between the two scattered quarks.[16,17,53] The $t\bar{t}$ production and WW QCD backgrounds, on the other hand, involve color exchange between the incident partons and, as a result, gluon radiation into the central region dominates. This gluon radiation then results in substantial hadronic activity in the vicinity of the W decay leptons.

While a rapidity gap trigger should suppress the backgrounds well below the signal level, it is not practical at the LHC, due to the small signal rate and small survival probability of the signal. In order for a rapidity gap to be visible no additional scattering process may occur in the detector at the same time, neither in the same pp collision which produces the Higgs boson, nor by other proton pairs which collide in the same bunch crossing. The first condition is parametrized by the survival probability, P_s, which was discussed in Section 4.2, and which we expect to be below 10% at the LHC.[17,37,39] The second condition implies that one must run the LHC well below design luminosity, at an average of one pp scattering event per bunch crossing, or about $\mathcal{L} = 5 \cdot 10^{32} \mathrm{cm}^{-2} \mathrm{sec}^{-1}$. Even at this low luminosity only $P_1 = e^{-1} = 37\%$ of all bunch crossings have exactly one pp scattering event, leading to an effective yearly integrated luminosity of about 2 fb^{-1}. Given the signal cross section of 1.02 fb in the third column of Table 2 and an (optimistic) survival probability of $P_s = 10\%$, one would register only one Higgs signal event every five years! Note that the cuts imposed on the leptons and tagging-jet are not responsible for this negative result: 22% of all signal events are accepted by them.[18] It is the combination of small survival probability and additional effective luminosity reduction by a factor 50 which kills the signal. Given the small weak boson scattering cross section, any rapidity gap strategy at the LHC must raise this effective survival probability from 1/500 to something of order unity, i.e. it must work at full design luminosity and must tolerate the presence of an underlying event.

The way out may be to use minijets rather than soft hadrons to define the rapidity gap. Beyond the different angular distribution of gluons in signal and background events, a second distinction is the momentum scale Q of the hard process which governs the radiation. In longitudinal weak boson scattering the color charges, carried by the incident quarks, receive momentum transfers given by the transverse momenta of the final state quarks, which typically are in the $Q = 30$ to 80 GeV range. For the background processes, on the other hand, the color charges receive a much larger momentum kick, of the order of the weak boson pair mass or even the parton center of mass energy of the event, i.e. $Q \approx 1$ TeV. Extra parton emission is suppressed by a factor $f_s = \alpha_s \ln (Q^2/p_{T,\min}^2)$, where $p_{T,\min}$ is the minimal transverse momentum required for a parton to qualify as a jet. The jet transverse momentum scale below which multiple minijet emission must be expected is set by $f_s = \mathcal{O}(1)$, and this scale is in the 30–50 GeV range for the backgrounds but well below 10 GeV for the signal.

For a more precise determination of the typical minijet p_T scale we must carry signal and background calculations still one order (in α_s) higher, i.e. the emission of one additional parton must be included. Thus we are led to consider $qq \to qqWWg$ and crossing related processes[54] for the weak boson scattering signal, and for the backgrounds $t\bar{t}jj$ events[55] and $WWjj$ events[56] must be simulated. Again the methods discussed in Section 3 are very useful in performing these tasks. The results of these calculations confirm the qualitative arguments made above. For the hard lepton and tagging-jet cuts of Eqs. (80)–(83), the $WWjj$ cross section, for example, is equal to the lowest order WWj cross section for a minimal parton transverse momentum of 37 GeV. Thus multiple minijets in the 20–50 GeV range are expected for the WW QCD back-

ground. Similar results are found for the $t\bar{t}$ background while this "saturation scale" for the signal is well below 10 GeV.

For a quantitative estimate of the minijet emission probability, we must use the higher order programs (which include emission of soft partons) in regions of phase space where the $n+1$ jet cross section saturates the rate for the hard process with n jets. As the p_T of the softest jet is lowered to values where $\sigma(n+1 \text{ jet}) \simeq \sigma(n \text{ jet})$, fixed order perturbation theory breaks down and multiple soft gluon emission (with resummation of collinear singularities into quark and gluon structure functions, etc.) needs to be considered in a full treatment. For the complex processes considered here such calculations are not yet possible. Instead one can employ the so called "truncated shower approximation" (TSA) to normalize the higher order emission calculations.[57] The tree-level $n+1$ jet differential cross section $d\sigma(n+1\,j)_{\text{TL}}$ is replaced by

$$d\sigma(n+1\,j)_{\text{TSA}} = d\sigma(n+1\,j)_{\text{TL}} \left(1 - e^{-p_{Tj,min}^2/p_{TSA}^2}\right) \;, \tag{84}$$

with the parameter p_{TSA} properly chosen to correctly reproduce the lower order n jet cross section when integrated over a given phase space region of this hard process. Here $p_{Tj,min}$ is the smallest transverse momentum of any of the final state massless partons. As $p_{Tj,min} \to 0$ the final factor in Eq. (84) acts as a regulator, which allows to integrate the $n+1$ parton cross section over the full phase space region and simulate n-jet and $n+1$-jet events simultaneously.

The results of such a calculation[18] are depicted in Fig. 17. The angular distribution of the jet (parton with $p_T > 20$ GeV) which is closest to the leptons (more precisely, closest to the average lepton rapidity $\bar{\eta} = (\eta_{\ell+} + \eta_{\ell-})/2$) is shown in Fig. 17(a). The background processes favor emission close to the leptons. For the Higgs signal this closest jet is typically the second quark in the $qq \to qqH$ process and not soft gluon radiation. It is this different angular distribution which is at the heart of the rapidity gap trigger.

A good compromise between strong background rejection and high signal acceptance is achieved by vetoing jets in the veto region defined by

$$p_{Tj}^{\text{veto}} > p_{T,\text{veto}} \;, \qquad\qquad \eta_j^{\text{veto}} \varepsilon \;\; [\eta_\ell^{\text{min}} - 1.7, \eta_j^{\text{tag}}] \;\; \text{or} \;\; [\eta_j^{\text{tag}}, \eta_\ell^{\text{max}} + 1.7] \;. \tag{85}$$

The veto probability as a function of the cut value $p_{T,\text{veto}}$ is shown in Fig. 17(b). Even though these results were obtained in the truncated shower approximation and a more precise modeling is needed, they clearly demonstrate that, in the central region, the backgrounds have a much higher probability to produce additional minijets from QCD radiation than the weak boson scattering signal. Even for the $t\bar{t}$ background, where a strong suppression is obtained by vetoing the central b-quark jets arising from the top decays, the veto on the jet activity from soft QCD radiation provides an additional suppression by a factor 2 for $p_{T,\text{veto}} = 20$ GeV. Final cross section values for signal and backgrounds are given in the last column of Table 2. Should minijet vetoing be possible at the LHC for even smaller $p_{T,\text{veto}}$ values then the $t\bar{t}$ background to $H \to WW$ events can effectively be eliminated.
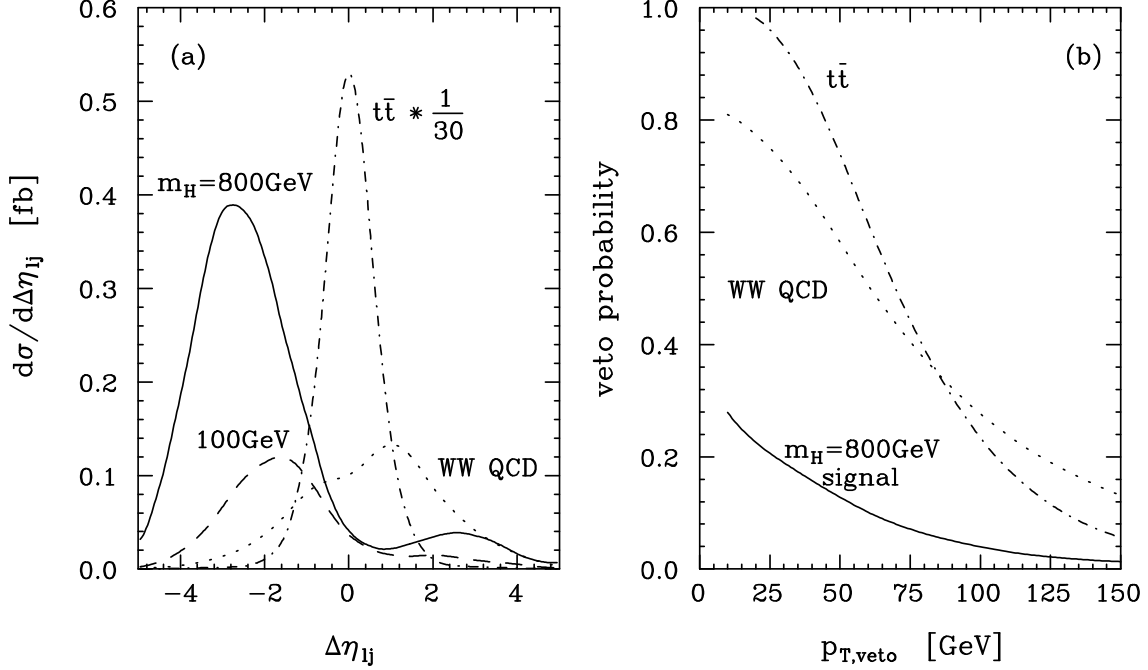
Fig. 17. Rapidity and transverse momentum distributions of secondary jets. In (a) $\Delta\eta_{\ell j}$ measures the pseudorapidity distance of the jet closest to the leptons from the average lepton rapidity $\bar\eta$. Negative values of $\Delta\eta_{\ell j}$ correspond to soft jets on the opposite side of the leptons with respect to the tagging jet. The dashed line shows the distribution for the electroweak background as defined by the $m_H = 100$ GeV case. The $t\bar t jj$ background has been scaled down by a factor 30. The probability to find a veto jet candidate above a transverse momentum $p_{T,\mathrm{veto}}$, in the veto region of Eq. (85), is shown in (b). From Ref. 18.

6.   Conclusions

Rapidity gaps in hard dijet events at the Tevatron and minijet patterns in weak boson scattering at the LHC have their common origin in processes which are dominated by t-channel color singlet exchange. Both can be understood in terms of soft gluon radiation patterns which are determined by the color structure of the underlying hard scattering event. At the lower energy of the Tevatron the soft gluon radiation pattern is reflected in the distribution of soft hadrons in events without a residual minimum bias event (underlying event). Going up one order of magnitude to LHC energy, "soft gluons" can be hard enough to be seen as distinct minijets, and this opens new strategies for the study of weak boson scattering events.

The theoretical description of these multi-parton processes has become possible with the advent of amplitude techniques. By directly evaluating polarization amplitudes numerically, fast numerical programs can be designed which remain efficient for processes with large numbers of Feynman graphs. In addition, code generation for SM processes has now been automated and this allows us to concentrate on the physics

issues in the analysis of multi-parton processes.

Via the study of rapidity gap events we are obtaining important information for future LHC physics studies already now at the Tevatron. Similarly, multiple minijet emission, which is expected to be quite common at the LHC, can already now be studied in the hardest "dijet" events at the Tevatron.[58,59] Both examples show the important interplay between present experiments and new theoretical ideas and tools in multi-parton analysis. Some of these developments were motivated by the search for new physics at future colliders. At the same time they aid in the preparation of experiments at these machines.

Acknowledgements

References

1. UA1 Collaboration, G. Arnison et al., Phys. Lett. **122B** (1983) 103; UA2 Collaboration, M. Banner et al., Phys. Lett. **122B** (1983) 476.
2. CDF Collaboration, F. Abe et al., Phys. Rev. **D50** (1994) 2966; Phys. Rev. **D52** (1995) 2605.
3. CDF Collaboration, F. Abe et al., Phys. Rev. Lett. **74** (1995) 2626.
4. D0 Collaboration, S. Abachi et al., Phys. Rev. Lett. **74** (1995) 2422; Phys. Rev. Lett. **74** (1995) 2632; Phys. Rev. **D52** (1995) 4877.
5. For a recent review see e.g. X. Tata, lectures given at TASI 1995, Univ. of Hawaii preprint UH-511-833-95 (1995), hep-ph/9510287.
6. P. De Causmaeker, R. Gastmans, W. Troost, and T. T. Wu, Nucl. Phys. **B206** (1982) 53; F. A. Berends, R. Kleiss, P. De Causmaeker, R. Gastmans, W. Troost, and T. T. Wu, Nucl. Phys. **B206** (1982) 61; **B264** (1986) 265 and references therein; D. Danckaert, P. De Causmaeker, R. Gastmans, W. Troost, and T. T. Wu, Phys. Lett. **114B** (1982) 203.
7. Z. Xu, Da-Hua Zhang, and L. Chang, Tsinghua University Preprint, Beijing, TUTP-84/4, TUTP-84/5, TUTP-84/6, and Nucl. Phys. **B291** (1987) 392; J. F. Gunion and Z. Kunszt, Phys. Lett. **161B** (1985) 333; R. Kleiss and W. J. Stirling, Nucl. Phys. **B262** (1985) 167.
8. K. Hagiwara and D. Zeppenfeld, Nucl. Phys. **B274** (1986) 1; ibid. **B313** (1989) 560.
9. H. Murayama, I. Watanabe, and K. Hagiwara, KEK Report 91-11 (1992).
10. T. Stelzer and W. F. Long, Comput. Phys. Commun. **81** (1994) 357.
11. For a recent review see e.g. J. Bagger et al., Phys. Rev. **D49** (1994) 1246; Phys. Rev. **D52** (1995) 3878.
12. R. N. Cahn et al., Phys. Rev. **D35** (1987) 1626; V. Barger et al., Phys. Rev. **D37** (1988) 2005; R. Kleiss and W. J. Stirling, Phys. Lett. **200B** (1988) 193.
13. U. Baur and E. W. N. Glover, Nucl. Phys. **B347** (1990) 12; U. Baur and E. W. N. Glover, Phys. Lett. **B252** (1990) 683; D. Froideveaux, in *Proceedings of the ECFA Large Hadron Collider Workshop*, Aachen, Germany, 1990, edited by G. Jarlskog and D. Rein (CERN report 90-10, Geneva, Switzerland, 1990), Vol II, p. 444; M. H. Seymour, ibid, p. 557; V. Barger, K. Cheung, T. Han, J. Ohnemus, and D. Zeppenfeld, Phys. Rev. **D44** (1991) 1426.
14. V. Barger, K. Cheung, T. Han, and R. J. N. Phillips, Phys. Rev. **D42** (1990) 3052.
15. V. Barger, K. Cheung, T. Han, and D. Zeppenfeld, Phys. Rev. **D44** (1991) 2701; **D48** (1993) 5444E; **D48** (1993) 5433.
16. Y. L. Dokshitzer, V. A. Khoze, and S. Troyan, in *Proceedings of the 6th International Conference on Physics in Collisions*, (1986) ed. M. Derrick (World Scientific, Singapore, 1987) p.365.
17. J. D. Bjorken, Int. J. Mod. Phys. **A7** (1992) 4189; Phys. Rev. **D47** (1993) 101; preprint SLAC-PUB-5823 (1992).
18. V. Barger, R. J. N. Phillips, and D. Zeppenfeld, Phys. Lett. **B346** (1995) 106.
19. D0 Collaboration, S. Abachi et al., Phys. Rev. Lett. **72** (1994) 2332.
20. CDF Collaboration, F. Abe et al., Phys. Rev. Lett. **74** (1995) 855.

21. D0 Collaboration, S. Abachi et al., Phys. Rev. Lett. **76** (1996) 734.
22. P. Nason, S. Dawson, and R. K. Ellis, Nucl.Phys. **B303** (1988) 607; E. Laenen, J. Smith, and W. L. van Neerven, Nucl.Phys. **B369** (1992) 543; Phys. Lett. **B321** (1994) 254.
23. S. Catani, M. Mangano, P. Nason, and L.Trentadue, preprint CERN-TH-96-21 (1996), hep-ph/9602208.
24. V. Barger, T. Han, J. Ohnemus, and D. Zeppenfeld, Phys. Rev. **D40** (1989) 2888; F. A. Berends, W. T. Giele, and H. Kuijf, Nucl. Phys. **B321** (1989) 39; F. A. Berends et al., Phys. Lett. **B224** (1989) 237.
25. F. A. Berends, H. Kuijf, B. Tausk, and W. T. Giele, Nucl. Phys. **B357** (1991) 32.
26. K. Kleinknecht, Talk presented at the *XXXth Rencontre de Moriond "Electroweak interactions and unified theories"*, Les Arcs, Savoie, 11–18 March 1995.
27. G. Peter Lepage, J. Comput. Phys. **27**, 192 (1978).
28. S. Kawabata, Comput. Phys. Commun. **41** (1986) 127.
29. U. Baur and D. Zeppenfeld, Phys. Rev. Lett. **75** (1995) 1002; E. N. Argyres et al., Phys. Lett. **B358** (1995) 339.
30. K. Hagiwara et al., Nucl. Phys. **B282** (1987) 253.
31. J. Kublbeck, M. Böhm, and A. Denner, Comput. Phys. Commun. **60** (1990) 165.
32. R. Mertig, M. Böhm, and A. Denner, Comput. Phys. Commun. **64** (1991) 345; A. Hsieh and E. Yehudai, Comput. Phys. **6** (1992) 253; T. Ishikawa et al., KEK Report 92-19 (1993); E. E. Boos et al., Int. J. Mod. Phys. **C5** (1994) 615.
33. V. Barger et al., Phys. Lett. **B338** (1994) 336.
34. D. Zeppenfeld, Int. J. Mod. Phys. **A3** (1988) 2175; K. Hagiwara and D. Zeppenfeld, Nucl. Phys. **B313** (1989) 560; V. Barger, A. L. Stange, and R. J. N. Phillips, Phys. Rev. **D45** (1992) 1751.
35. H. Chehime and D. Zeppenfeld, preprint MAD/PH/814 (1994), hep-ph/9401244.
36. Y. L. Dokshitzer *et al.*, *Rev. Mod. Phys.* **60** (1988) 373, and references therein.
37. R. S. Fletcher and T. Stelzer, Phys. Rev. **D48** (1993) 5162.
38. H. Chehime et al., Phys. Lett. **B286** (1992) 397.
39. E. Gotsman, E. M. Levin, and U. Maor, Phys. Lett. **B309** (1993) 199.
40. H. Chehime and D. Zeppenfeld, Phys. Rev. **D47** (1993) 3898.
41. F. E. Low, Phys. Rev. **D12** (1975) 163; S. Nussinov, Phys. Rev. Lett. **34** (1975) 1286.
42. See e.g. J. R. Cudell and B. U. Nguyen, Nucl. Phys. **B420** (1994) 669 and references therein.
43. P. V. Landshoff and O. Nachtmann, Z. Phys. **C35** (1987) 405;
44. F. Halzen, G. I. Krein, and A. A. Natale, Phys. Rev. **D47** (1992) 295; M. B. Gay Ducati, F. Halzen, and A. A. Natale, Phys. Rev. **D48** (1993) 2324.
45. For a more complete discussion see e.g. J. F. Gunion, H. E. Haber, G. Kane, and S. Dawson, *The Higgs Hunter's Guide*, Addison-Wesley (1990).
46. J. F. Gunion, A. Stange, and S. S. D. Willenbrock, preprint UCD-95-28 (1995), hep-ph/9602238.
47. D. A. Dicus and R. Vega, Phys. Rev. Lett. **57** (1986) 1110; Phys. Rev. **D37** (1988) 2427; J. F. Gunion, J. Kalinowski, and A. Tofighi-Niaki, Phys. Rev. Lett. **57** (1986) 2351; U. Baur and E. W. N. Glover, Phys. Lett. **B252** (1990) 683.

48. D. A. Dicus and V. S. Mathur, Phys. Rev. **D7** (1973) 3111; B. W. Lee, C. Quigg, and H. Thacker, Phys. Rev. **D16** (1977) 1519; M. Veltman, Acta Phys. Pol. **B8** (1977) 475; M. S. Chanowitz and M. K. Gaillard, Nucl. Phys. **B261** (1985) 379.
49. See e.g. V. Barger and R. Phillips, *Collider Physics*, Addison-Wesley (1987).
50. V. Barger et al., Phys. Rev. **D46**, 2028 (1992).
51. D. Dicus, J. F. Gunion, and R. Vega, Phys. Lett. **B258**, 475 (1991); D. Dicus, J. F. Gunion, L. H. Orr, and R. Vega, Nucl. Phys. **B377**, 31 (1991).
52. G. Ciapetta and A. DiCiaccio, in *Proceedings of the ECFA Large Hadron Collider Workshop*, Aachen, Germany, 1990, edited by G. Jarlskog and D. Rein (CERN report 90-10, Geneva, Switzerland, 1990), Vol II, p. 155.
53. J. F. Gunion *et al.*, *Phys. Rev.* **D40** (1989) 2223.
54. A. Duff and D. Zeppenfeld, Phys. Rev. **D50** (1994) 3204.
55. A. Stange, private communication.
56. V. Barger, T. Han, J. Ohnemus, and D. Zeppenfeld, Phys. Rev. **D41** (1989) 2782.
57. V. Barger and R. J. N. Phillips, Phys. Rev. Lett. **55** (1985) 2752; H. Baer, V. Barger, H. Goldberg, and R. J. N. Phillips, Phys. Rev. **D37** (1988) 3152.
58. CDF Collaboration, F. Abe et al., Phys. Rev. Lett. **75** (1995) 608.
59. D. Summers and D. Zeppenfeld, preprint MADPH-95-904 (1995), hep-ph/9509206.